PHYSICAL REVIEW E VOLUME 49, NUMBER 5 MAY 1994

Late-stage phase separation: Dynamics, spatial correlations, and structure functions

Norio Akaiwa* and P.W. Voorhees
Department of Materials Science and Engineering, Northwestern University, Evanston, Illinois 60208

(Received 9 November 1993)

Particle coarsening in the late stage was investigated using numerical simulations. The multiparticle diffusion problem was solved using a multipole expansion method which is valid to an arbitrary order of the expansion. The simulations were performed using both monopole and monopole plus dipole approximations. We found that the monopole approximation yields a good description of the diffusion field up to a volume fraction of approximately 0.1. Beyond this volume fraction, particle migration induced by interparticle diffusional interactions plays an important role. The simulations were performed using two different initial spatial distributions. Despite the different initial states of the system, we find that the spatial correlation functions evolve to unique scaled time independent forms. These spatial correlation functions show that depletion zones exist between small particles and that the density of small particles near large particles is less than that of a random spatial distribution. A scaled time independent structure function similar to that observed experimentally was found. The slope of the structure function in a log-log plot is close to 4 at small wave numbers and is −4 at very large wave numbers. Oscillations in the structure function, which are related to the spherical shape and size distribution of particles, are present at large wave numbers. The rate constant of the cubic growth law and the scaled particle size distribution are also determined.

PACS number(s): 64.60.My

I. INTRODUCTION

In the late stage of a first-order phase transition, the evolution of the two-phase mixture is driven by the reduction in the excess energy associated with the interfaces between the two phases. The reduction in total interfacial energy results in an increase in the average size of the minority phase domains. This Ostwald ripening or coarsening process takes place by the diffusion of heat or mass from regions of interface with high interfacial curvature to regions of interface with low interfacial curvature. Here we will consider the dynamics of coarsening following an off-critical quench wherein the system is composed of an array of second-phase domains.

A complete theory of the coarsening of a system of spherical particles was developed by Lifshitz and Slyozov [1] and by Wagner [2] (the LSW theory). They found that in the long-time limit the cube of the average particle size should increase linearly with time during coarsening, and that when the particle size distribution is scaled by the time dependent average particle radius, it should assume a unique time independent form for all initial conditions. However, the primary assumption in the LSW theory is that the concentration field surrounding a particle is given by a solution of the diffusion equation for an isolated spherical particle. This means that diffusional interactions between particles are not taken into account, and thus the theory is valid only in the limit of a zero volume fraction of the second-phase. Experiments have shown that amplitude of the temporal power law for the average particle size, the rate constant, is much higher and the particle size distribution function is broader than those predicted by the LSW theory and as volume fraction increases, these discrepancies become larger [3].

At nonzero volume fractions, the diffusion field assumed by LSW is perturbed due to the existence of other particles. Qualitatively we would expect that the concentration gradient at the particle-matrix interface to become steeper as volume fraction of particles increases. Thus, the kinetics of the coarsening process should increase as the volume fraction increases. All treatments of the coarsening process predict that the presence of a nonzero volume fraction does not alter the exponent of the temporal power laws, but does affect the amplitude of these power laws. The influence of a nonzero volume fraction of coarsening phase has been investigated using mean-field theories [4–7], statistical mechanical theories [8–12], and numerical simulations [7,13–16]. The predictions of all of these theories reduce to the LSW results in the limit of zero volume fraction. However, many of these theories yield very different predictions. For example, Marder's theory [12] yields a rate constant at a particular volume fraction which is as much as an order of magnitude larger than other theories. In addition, all of the statistical mechanical theories and simulations are based upon a solution to the diffusion field in the matrix using monopole sources or sinks of mass located at the center of the particles. This implies that the theories are valid only at low volume fractions of coarsening phase. The approximate value of the limiting volume fraction is unknown. Generally, the mean-field theories give higher rate constants than those of the statistical mechanical theories.

The importance of the particle spatial correlations on the dynamics of coarsening has recently been recognized [9,15,17]. It is clear that for the evolution of the system to be described by temporal power laws, the particle

---

*Present address: Department of Applied Mathematics, Firestone Laboratory, California Institute of Technology, Pasadena, CA 91125.

1063-651X/94/49(5)/3860(21)/$06.00

spatial correlation functions must have specific time independent forms when scaled by a time dependent length scale, such as the average particle size. However, the nature of the particle spatial correlations created during coarsening is not well understood. Experiments have shown that scaled time independent spatial correlations do indeed exist. Many workers have shown that the structure function, which is measured using small angle x-ray, neutron, or light scattering, assumes a time independent form when scaled by a time dependent length [18–27]. While it is clear that the structure function depends on the spatial correlations, using this measured structure function to determine the spatial correlation function is problematical, as the structure function depends on both the particle spatial correlations and the particle size distribution. In principle, information on the particle correlations can be obtained by examining the small wave number behavior of the structure function. However, this can be difficult due to the strong background intensity of the transmitted beam. Nevertheless, attempts have been made to reproduce the measured structure function by assuming specific forms for the particle size distribution and the particle spatial correlation functions [23,24,28–30]. In these works, the spatial correlations are modeled by assuming that a depletion zone of a certain size exits surrounding each particle. Although it is possible to reproduce the measured structure function by this method, the existence of depletion zones surrounding particles has not been confirmed experimentally, due to the difficulty in measuring correlation functions in real space in three dimensions. However, there has been progress along these lines by Krichevsky and Stavans [31] for coarsening in a two-dimensional system. They measured the radial distribution function and pair correlation functions, and showed that the probability of finding small particles near a large particle is larger than that of finding small or large particles near each other. Theoretically, Beenakker [15] calculated moments of the pair distribution function found from computer simulations using the monopole approximation and found that the particle spatial correlations are not simple hard sphere correlations. Marder [12] developed a theory which accounts for the effects of spatial correlations between coarsening particles; however, the particle correlations are much different from those found by Beenakker at small particle separations. Tokuyama *et al.* [32,33] calculated the structure function in the late stage, and showed that the structure function depends on the wave number k as k^4 for small k and k^{-4} for large k. However, the calculated structure functions are broader than those obtained by experiments. Yao *et al.* [7] calculated the structure functions from their simulations. Unfortunately, due to the small size of the system employed in their simulations their scaled structure functions at low wave numbers are time dependent, and thus the system is not in the scaling region.

Here we discuss the effects of a high volume fraction of coarsening phase on the dynamics of coarsening. We have investigated the coarsening process via numerical simulations, as these allow us to examine the effects of many body diffusional interactions on the coarsening process without any *a priori* assumptions on the form of the particle spatial correlations. We have determined particle correlation functions in addition to the amplitudes of the temporal power law for the average particle size and scaled time independent particle size distribution functions. The radial distribution function, pair correlation functions, and the structure function are used to characterize these spatial correlations. Simulations with different initial particle spatial distributions, but the same particle size distribution, are performed to test the existence of time independent scaled spatial correlations. As mentioned above, in all the previous simulations [7,13–16], the diffusion field is calculated using the monopole approximation. Since the validity of the monopole approximation is restricted to low volume fractions, the effect of dipole sources and sinks is examined. Finally, we also consider the validity of assuming that the minority phase particles are spherical in these multiparticle systems.

II. MATHEMATICAL FORMULATION OF THE COARSENING PROBLEM

In reality, the morphology of the individual second-phase domains is not fixed. Thus, a description of the coarsening process at high volume fraction involves a solution to a multiparticle free-boundary problem. As solutions to free-boundary problems in three dimensions with large numbers of particles are quite difficult, we shall assume that the particles are spherical. However, to obtain a self-consistent theory, we will justify this assumption later.

Thus, we take the system to consist of a large spherical external boundary S, with N spherical particles embedded in the matrix. We shall frame our description in terms of a binary stress-free two-phase mixture in which coarsening takes place by the flow of mass from small particles to large particles. Our interest is restricted to the late stage where the volume fraction is nearly the equilibrium value, or the supersaturation is very small. Thus, to a high degree of approximation the concentration field in the matrix is given by a solution to the steady state diffusion equation,

$$\nabla^2 C = 0, \tag{2.1}$$

where C is the concentration, in mole fraction of component 1. Local equilibrium is assumed to exist at the particle-matrix interface so that the concentration is given by the Gibbs-Thomson equation,

$$C(R) = C_m^{\mathrm{eq}}\left(1 + \frac{\alpha}{R}\right) \tag{2.2}$$

where R is the radius of the particle, C_m^{eq} is the equilibrium concentration at a planar interface in the matrix phase, the capillary length α for the matrix phase is given by

$$\alpha = \frac{2\sigma v_m}{C_m^{\mathrm{eq}}(C_p^{\mathrm{eq}} - C_m^{\mathrm{eq}})G_m''} \tag{2.3}$$

σ is the interfacial energy, v_m is the molar volume of the matrix phase, C_p^{eq} is the equilibrium concentration at a planar interface in the particle phase, and G''_m is the second derivative of the molar free energy with respect to composition of the matrix phase. The capillary length is a material constant with a typical value of $10^{-8} - 10^{-10}$ m. Although Eq. (2.2) is not valid for small particles, since the concentration becomes infinite as R goes to zero, the fraction of these particles at any moment is sufficiently small so that Eq. (2.2) is assumed to be valid for all particles. The flux conservation condition at each point on the interface of a particle is

$$(C_p^{\rm eq} - C_m^{\rm eq})\mathcal{V}_n = D\frac{\partial C}{\partial n}, \tag{2.4}$$

where $\mathcal{V}_n$ is the normal velocity of the interface, D is the diffusion coefficient in the matrix phase, $\mathbf{n}$ is a normal to the interface which is directed from the particle toward the matrix, and $\partial/\partial n$ denotes the derivative in the direction of $\mathbf{n}$. For a spherical particle, $\mathcal{V}_n$ is given by

$$\mathcal{V}_n = \frac{dR}{dt}. \tag{2.5}$$

Mass is conserved in the system so that the normal derivative of the concentration is zero at each point on the external boundary,

$$\frac{\partial C}{\partial n} = 0 \qquad \text{on } S, \tag{2.6}$$

where $\mathbf{n}$ is the normal to the external sphere, which is directed inward, toward the matrix.

The problem can be recast in the following dimensionless variables,

$$u = \frac{R_0(C - C_m^{\rm eq})}{\alpha C_m^{\rm eq}}, \tag{2.7}$$

$$r = \frac{R}{R_0}, \tag{2.8}$$

$$t' = \frac{C_m^{\rm eq} D\alpha}{(C_p^{\rm eq} - C_m^{\rm eq})R_0^3}t, \tag{2.9}$$

where R_0 is the initial average radius. Dropping the prime on t, Eqs. (2.1), (2.2), (2.4), and (2.6) become

$$\nabla^2 u = 0, \tag{2.10}$$

$$u(r) = \frac{1}{r}, \tag{2.11}$$

$$v_n = \frac{\partial u}{\partial n}, \tag{2.12}$$

$$\frac{\partial u}{\partial n} = 0 \qquad \text{on } S, \tag{2.13}$$

where v_n is the dimensionless normal velocity of the interface. Equations (2.10)–(2.13) are the governing equations of the problem. This is a classical multiparticle diffusion problem and has been investigated by other workers. Beenakker and Ross [34] expressed the solution to this system using a set of irreducible tensors. This method was extended for nonconstant interfacial concentration by Abinandanan and Johnson [35,36]. Imaeda and Kawasaki [37] solved this problem for the case of nonspherical particles using a multipole expansion method.

Here we reformulate the diffusion problem into an integral form which automatically accounts for the boundary conditions. Applying Green's formula for the matrix,

$$\begin{aligned}\int_{V_m} &[u(\mathbf{q})\nabla^2 g(\mathbf{p},\mathbf{q}) - \nabla^2 u(\mathbf{q}) g(\mathbf{p},\mathbf{q})]\, d\mathbf{Q}\\ &= -\sum_j^N \int_{S_j} \left(u(\mathbf{q})\frac{\partial g(\mathbf{p},\mathbf{q})}{\partial n_q} - \frac{\partial u(\mathbf{q})}{\partial n_q} g(\mathbf{p},\mathbf{q}) \right) d\mathbf{q}\\ &\quad - \int_S \left(u(\mathbf{q})\frac{\partial g(\mathbf{p},\mathbf{q})}{\partial n_q} - \frac{\partial u(\mathbf{q})}{\partial n_q} g(\mathbf{p},\mathbf{q}) \right) d\mathbf{q},\end{aligned} \tag{2.14}$$

where V_m is the volume of the matrix, S_j is the surface of the particle j, $\mathbf{p}$ is a field point, $\mathbf{q}$ is an integration point, $g(\mathbf{p},\mathbf{q})$ is defined as

$$g(\mathbf{p},\mathbf{q}) = \frac{1}{|\mathbf{p} - \mathbf{q}|}, \tag{2.15}$$

and $g(\mathbf{p},\mathbf{q})$ satisfies Poisson's equation,

$$\nabla^2 g(\mathbf{p},\mathbf{q}) = -4\pi\delta(\mathbf{p} - \mathbf{q}), \tag{2.16}$$

where $\delta(\mathbf{p} - \mathbf{q})$ is a Dirac delta function. Using the properties of the delta function, the first part of the left-hand side of Eq. (2.14) becomes

$$\begin{aligned}\int_{V_m} &u(\mathbf{q})\nabla^2 g(\mathbf{p},\mathbf{q}) d\mathbf{Q}\\ &= -4\pi \int_{V_m} u(\mathbf{q})\delta(\mathbf{p} - \mathbf{q}) d\mathbf{Q}\\ &= \begin{cases} -4\pi u(\mathbf{p}), & \mathbf{p} \text{ in the matrix},\\ -2\pi u(\mathbf{p}), & \mathbf{p} \text{ on } S_j \text{ or } S,\\ 0, & \mathbf{p} \text{ inside a particle}. \end{cases}\end{aligned} \tag{2.17}$$

Since the concentration in the matrix at the interface is constant, u_j, the value of the double layer potential due to the particles, the first term on the right-hand side of Eq. (2.14), becomes [38],

$$\begin{aligned}\int_{S_j} &u(\mathbf{q})\frac{\partial g(\mathbf{p},\mathbf{q})}{\partial n_q} d\mathbf{q}\\ &= \begin{cases} -4\pi u_j, & \mathbf{p} \text{ inside particle } j,\\ -2\pi u_j, & \mathbf{p} \text{ on } S_j,\\ 0, & \mathbf{p} \text{ in the matrix}. \end{cases}\end{aligned} \tag{2.18}$$

Substituting Eqs. (2.10), (2.13), (2.17), and (2.18) into Eq. (2.14) yields

$$u(\mathbf{p}) = -\frac{1}{4\pi}\sum_{j}^{N}\int_{S_j}\sigma(\mathbf{q})g(\mathbf{p},\mathbf{q})d\mathbf{q} + u_{00}, \tag{2.19}$$

where $\sigma(\mathbf{q})$ is the single layer density,

$$\sigma(\mathbf{q}) = \frac{\partial u(\mathbf{q})}{\partial n_q}, \tag{2.20}$$

and u_{00} is a constant. To arrive at Eq. (2.20), we have used the asymptotic form for the contribution to the concentration from the external surface which is found in the limit where the radius of the external sphere is infinitely large [39],

$$\frac{1}{4\pi}\int_{S} u(\mathbf{q})\frac{\partial g(\mathbf{p},\mathbf{q})}{\partial n_q}d\mathbf{q} = u_{00} + O\left(\frac{p}{R_s}\right), \tag{2.21}$$

where R_s is the radius of the external sphere and $p = |\mathbf{p}|$.

Equation (2.19) is valid when $\mathbf{p}$ is in the matrix, on S_j and also inside S_j. Equation (2.19) gives the potential inside S_j to be a *constant* whose value can be chosen to be given by the Gibbs-Thomson boundary condition, Eq. (2.11). In reality, the concentration inside a particle is not constant, as the concentration within a particle changes with its radius. However, this effect is small for most systems and thus we shall neglect it. Equation (2.19) is the integral form of the concentration, or, using the electrostatic analogy, the potential. The potential at $\mathbf{p}$ is given by the sum of the single layer potentials generated by the density $\sigma(\mathbf{q})$ on the surface of the particles and a constant. Now the problem is to find $\sigma(\mathbf{q})$. Using the definition of $\sigma(\mathbf{q})$, Eq. (2.20), an equation for the single layer density can be found by taking the surface normal derivative of Eq. (2.19) on particle j,

$$\frac{\partial u(\mathbf{p})}{\partial n_p} = \frac{\partial}{\partial n_p}\left(-\frac{1}{4\pi}\sum_{k}^{N}\int_{S_k}\sigma(\mathbf{q})g(\mathbf{p},\mathbf{q})d\mathbf{q}\right), \quad \mathbf{p} \text{ on } S_j. \tag{2.22}$$

When both the field point and the integration point are located on particle j, $g(\mathbf{p},\mathbf{q})$ is singular. However, the integral is defined in this case and the normal derivative is given by the boundary relation [38],

$$\frac{\partial}{\partial n_p}\int_{S_j}\sigma(\mathbf{q})g(\mathbf{p},\mathbf{q})d\mathbf{q} = \int_{S_j}\sigma(\mathbf{q})\frac{\partial g(\mathbf{p},\mathbf{q})}{\partial n_p}d\mathbf{q} - 2\pi\sigma(\mathbf{p}). \tag{2.23}$$

Using Eq. (2.23), Eq. (2.22) becomes

$$\frac{\partial u(\mathbf{p})}{\partial n_p} = -\frac{1}{4\pi}\left(\int_{S_j}\sigma(\mathbf{q})\frac{\partial g(\mathbf{p},\mathbf{q})}{\partial n_p}d\mathbf{q} - 2\pi\sigma(\mathbf{p})\right) - \frac{1}{4\pi}\sum_{k\neq j}^{N}\int_{S_k}\sigma(\mathbf{q})\frac{\partial g(\mathbf{p},\mathbf{q})}{\partial n_p}d\mathbf{q}. \tag{2.24}$$

Rewriting Eq. (2.24) using Eq. (2.20) yields

$$\sigma(\mathbf{p}) = -\frac{1}{2\pi}\sum_{k}^{N}\int_{S_k}\sigma(\mathbf{q})\frac{\partial g(\mathbf{p},\mathbf{q})}{\partial n_p}d\mathbf{q}. \tag{2.25}$$

Equation (2.25) is the homogeneous Fredholm integral equation of the second kind. A solution of this equation gives a single layer density which yields a constant potential on the surface of every particle. The adjoint equation of Eq. (2.25) has N linearly independent solutions [40]. Therefore by the Fredholm theorems, Eq. (2.25) has N linearly independent solutions. We have N boundary conditions by Eq. (2.11), so that $\sigma(\mathbf{p})$ can be obtained by solving Eqs. (2.19) and (2.25) with Eq. (2.11). However, there is a constant in Eq. (2.19), u_{00}, which has not been determined, and thus we need one more equation, which is given by the boundary condition on the external boundary, Eq. (2.13).

All of the integrals in Eqs. (2.19) and (2.25) are defined on spheres so that it is convenient to expand $\sigma(\mathbf{p})$, $g(\mathbf{p},\mathbf{q})$, and $\partial g(\mathbf{p},\mathbf{q})/\partial n_p$ in a series of spherical harmonics. We define the spherical harmonics as

$$Y_n^m(\mathbf{r}) = P_n^m(\cos\vartheta_r)e^{im\varphi_r}, \tag{2.26}$$

where θ_r and φ_r are the polar and azimuthal angles of a vector $\mathbf{r}$, and $P_n^m(\cos\theta_r)$ are the associated Legendre functions. We shall use $(\mathbf{r})$ in the argument of spherical harmonics as an abbreviation for the angles (θ_r, φ_r). Note that the spherical harmonics are not normalized, so the orthogonality integral becomes

$$\int_0^{2\pi}\int_0^{\pi} Y_n^m(\mathbf{r})Y_{n'}^{-m'}(\mathbf{r})\sin\vartheta_r d\vartheta_r d\varphi_r = \frac{(-1)^m 4\pi}{2n+1}\delta_{nn'}\delta_{mm'}, \tag{2.27}$$

where $\delta_{nn'}$ is the Kronecker delta.

Expanding $\sigma(\mathbf{p})$ in a series of spherical harmonics,

$$\sigma(\mathbf{p}) = \sum_{nm} Y_n^m(\mathbf{r}_j)a_{mn}^j, \quad \mathbf{p} \text{ on } S_j,\ j = 1,2,\ldots,N, \tag{2.28}$$

where $\mathbf{r}_j$ is a vector locating a point on the surface of particle j with its origin at the center of particle j, a_{mn}^j are constants, and

$$\sum_{nm} = \sum_{n=0}^{\infty}\sum_{m=-n}^{n}. \tag{2.29}$$

When the field point is on particle j and the integration point is on particle k, $g(\mathbf{p},\mathbf{q})$ is given by

$$g(\mathbf{p},\mathbf{q}) = \frac{1}{|\,\mathbf{r}_j - \mathbf{r}_k - \mathbf{d}_{jk}\,|}, \tag{2.30}$$

where $\mathbf{d}_{jk}$ is a vector emanating from the center of particle j to the center of particle k. Equation (2.30) can be expanded into a series of triple products of spherical harmonics (see the Appendix),

$$g(\mathbf{p},\mathbf{q}) = \sum_{nm}\sum_{n'm'}(-1)^{m+m'}K(n,m;n',m')\frac{r_j^n r_k^{n'}}{d_{jk}^{n+n'+1}} \times Y_{n+n'}^{-m+m'}(\mathbf{d}_{jk})Y_n^m(\mathbf{r}_j)Y_{n'}^{-m'}(\mathbf{r}_k), \tag{2.31}$$

where r_j, r_k, d_{jk} are norms of the vectors $\mathbf{r}_j$, $\mathbf{r}_k$, $\mathbf{d}_{jk}$, respectively, and

$$K(n,m;n',m') = (-1)^{n'} \frac{(n+n'+m-m')!}{(n+m)!(n'-m')!}. \qquad (2.32)$$

Using Eqs. (2.28) and (2.31) we can integrate the right-hand of Eq. (2.19),

$$\begin{aligned}\int_{S_k} &\sigma(\mathbf{q}) g(\mathbf{p},\mathbf{q}) d\mathbf{q} \\ &= \sum_{nm}\sum_{n'm'} \frac{(-1)^m 4\pi}{2n'+1} K(n,m;n',m') \frac{r_j^n r_k^{n'+2}}{d_{jk}^{n+n'+1}} \\ &\quad \times Y_{n+n'}^{-m+m'}(\mathbf{d}_{jk}) Y_n^m(\mathbf{r}_j) a_{m'n'}^k, \\ &\quad \mathbf{p} \text{ on } S_j,\ \mathbf{q} \text{ on } S_k. \end{aligned} \qquad (2.33)$$

Since the particles are spherical and the surface normal derivatives are taken outward to the particles, the normal derivative of the single layer potential on particle j is given by differentiating Eq. (2.33) with respect to r_j,

$$\begin{aligned}\int_{S_k} &\sigma(\mathbf{q}) \frac{\partial g(\mathbf{p},\mathbf{q})}{\partial n_p} d\mathbf{q} \\ &= \sum_{nm}\sum_{n'm'} \frac{(-1)^m 4\pi n}{2n'+1} K(n,m;n',m') \frac{r_j^{n-1} r_k^{n'+2}}{d_{jk}^{n+n'+1}} \\ &\quad \times Y_{n+n'}^{-m+m'}(\mathbf{d}_{jk}) Y_n^m(\mathbf{r}_j) a_{m'n'}^k, \\ &\quad \mathbf{p} \text{ on } S_j,\ \mathbf{q} \text{ on } S_k. \end{aligned} \qquad (2.34)$$

When both the integration point and the field point are located on the same particle, $g(\mathbf{p},\mathbf{q})$ is singular and cannot be expanded into a series of spherical harmonics. However, the single layer potential due to particle j for all $\mathbf{p}$ except on S_j is given by

$$\begin{aligned}\int_{S_j} &\sigma(\mathbf{q}) g(\mathbf{p},\mathbf{q}) d\mathbf{q} \\ &= \sum_{nm} \frac{4\pi}{2n+1} Y_n^m(\mathbf{p}) a_{mn}^j \\ &\quad \times \begin{cases} p^n / r_j^{n-1}, & \mathbf{p} \text{ inside } S_j, \\ r_j^{n+2}/p^{n+1}, & \mathbf{p} \text{ outside } S_j. \end{cases}\end{aligned} \qquad (2.35)$$

Since the single layer potential is continuous across the boundary, the integral on S_j can be evaluated by setting $p = r$ in Eq. (2.35),

$$\int_{S_j} \sigma(\mathbf{q}) g(\mathbf{p},\mathbf{q}) d\mathbf{q} = \sum_{nm} \frac{4\pi r_j}{2n+1} Y_n^m(\mathbf{p}) a_{mn}^j, \quad \mathbf{p} \text{ on } S_j. \qquad (2.36)$$

The normal derivative of the single layer potential is given by differentiating Eq. (2.35) by p. However, the normal derivative is discontinuous across the boundary. Using the boundary relation, Eq. (2.23), the outward normal derivative is given by the limit as $p \to r_j +$,

$$\begin{aligned}\lim_{p \to r_j +} &\left(\frac{\partial}{\partial \mathbf{n_p}} \sum_{nm} \frac{4\pi}{2n+1} Y_n^m(\mathbf{p}) \frac{r_j^{n+2}}{p^{n+1}} a_{mn}^j \right) \\ &= \int_{S_j} \sigma(\mathbf{q}) \frac{\partial g(\mathbf{p},\mathbf{q})}{\partial n_p} d\mathbf{q} - 2\pi\sigma(\mathbf{p}). \end{aligned} \qquad (2.37)$$

Thus,

$$\int_{S_j} \sigma(\mathbf{q}) \frac{\partial g(\mathbf{p},\mathbf{q})}{\partial n_p} d\mathbf{q} = -\sum_{nm} \frac{2\pi}{2n+1} Y_n^m(\mathbf{p}) a_{mn}^j, \quad \mathbf{p} \text{ on } S_j. \qquad (2.38)$$

All of the integrals in Eqs. (2.19) and (2.25) have been obtained.

Substituting Eqs. (2.34) and (2.38) into Eq. (2.25) yields,

$$\begin{aligned}\sigma(\mathbf{r}_j) &= \sum_{nm} \frac{1}{2n+1} Y_n^m(\mathbf{r}_j) a_{mn}^j \\ &\quad - \sum_{k \neq j}^{N} \sum_{nm} \sum_{n'm'} \frac{(-1)^m 2n}{2n'+1} K(n,m;n',m') \frac{r_j^{n-1} r_k^{n'+2}}{d_{jk}^{n+n'+1}} \\ &\quad \times Y_{n+n'}^{-m+m'}(\mathbf{d}_{jk}) Y_n^m(\mathbf{r}_j) a_{m'n'}^k, \\ &\quad \mathbf{p} \text{ on } S_j,\ j = 1,2,\ldots,N. \end{aligned} \qquad (2.39)$$

Using Eq. (2.28) and equating both sides of Eq. (2.39) for the same order of spherical harmonics with respect to r_j yields

$$\begin{aligned} b_{mn}^j &= -\sum_{k \neq j}^{N} \sum_{n'm'} (-1)^m \frac{2n+1}{2n'+1} K(n,m;n',m') \\ &\quad \times \frac{r_j^{n+1} r_k^{n'}}{d_{jk}^{n+n'+1}} Y_{n+n'}^{-m+m'}(\mathbf{d}_{jk}) b_{m'n'}^k \\ &\quad (n \geq 1), \end{aligned} \qquad (2.40)$$

where

$$b_{mn}^j = r_j^2 a_{mn}^j. \qquad (2.41)$$

Now the integral equation, Eq. (2.25), has been reduced to a system of linear equations. Note that Eq. (2.40) is not valid when $n = 0$, since both sides of Eq. (2.39) are equal when $n = 0$. n' in Eq. (2.40) can take the value 0, so this system of equations allows one to determine all the coefficients of the spherical harmonics once b_{00}^j is specified. Substituting Eqs. (2.33), (2.36), and (2.40) with the boundary condition, Eq. (2.11), into Eq. (2.19) gives

$$\begin{aligned}\frac{1}{r_i} &= -\frac{1}{r_i} b_{00}^i + u_{00} \\ &\quad - \sum_{j \neq i}^{N} \sum_{nm} \frac{(-1)^n r_j^n}{d_{ij}^{n+1}} \frac{1}{(2n+1)} Y_n^m(\mathbf{d}_{ij}) b_{mn}^j, \\ &\quad \text{on } S_i. \end{aligned} \qquad (2.42)$$

Since $\sigma(\mathbf{r}_j)$ has been chosen to satisfy Eq. (2.25), the concentration is constant at the interface and thus there are no terms in Eq. (2.42) which depend on the location of a point on the interface of a particle. The remaining unknown constant u_{00} is given by the boundary condition on the external boundary, Eq. (2.13), which gives [39],

$$\sum_{i}^{N} b_{00}^{i} = 0. \tag{2.43}$$

This is the well known global mass conservation constraint which is used to determine u_{00}. Thus, Eqs. (2.40), (2.42), and (2.43) yield an $\infty \times \infty$ set of linear equations for the constants b_{mn}^{j} and u_{00}.

The volumetric growth rate of a particle is given by

$$\frac{dV_j}{dt} = \int_{S_j} v_n(\mathbf{q})d\mathbf{q} \tag{2.44}$$

where V_j is the volume of particle j. Using Eqs. (2.12), (2.20), and (2.28) in Eq. (2.44) yields

$$\frac{dV_j}{dt} = 4\pi b_{00}^{j}. \tag{2.45}$$

From now on b_{00}, without the factor 4π, will be called the growth rate of the particle. The change in the vector locating the center of mass of particle j, $\delta\mathbf{R}_j$, in the time interval δt is given by

$$\delta\mathbf{R}_j = \frac{1}{V_j(t+\delta t)} \int_0^{2\pi}\int_0^{\pi}\int_0^{r_j+v_n\delta t} \mathbf{r}r^2 dr \sin\theta d\theta d\varphi - \frac{1}{V_j(t)} \int_0^{2\pi}\int_0^{\pi}\int_0^{r_j} \mathbf{r}r^2 dr \sin\theta d\theta d\varphi, \tag{2.46}$$

where $\mathbf{r}$ is a vector emanating from the center of a particle to a point on the interface at time t. Taking the limit $\delta t \to 0$ and using Eq. (2.12) yields the migration rate of a spherical particle due to a non-spherically-symmetric diffusion field,

$$\frac{d\mathbf{R}_j}{dt} = \frac{1}{V_j(t)} \int_0^{2\pi}\int_0^{\pi} \sigma\mathbf{r}r_j^2 \sin\theta d\theta d\varphi. \tag{2.47}$$

Using Eq. (2.28) in Eq. (2.47) yields the migration rate of the particle in terms of the coefficients of the $n = 1$ spherical harmonics,

$$\frac{d\mathbf{R}_j}{dt} = \frac{1}{r_j^2}\left[b_{11}^{j} - \tfrac{1}{2}b_{-11}^{j},\ i[b_{11}^{j} + \tfrac{1}{2}b_{-11}^{j}],\ b_{01}^{j}\right]. \tag{2.48}$$

This particle migration is strictly a manifestation of a non-spherically-symmetric diffusion field. Thus, this effect is generic to the coarsening process in high volume fraction systems and is not a result of a flow of the matrix.

III. NUMERICAL SIMULATION

If the expansion for the single layer density is truncated at n_c, one obtains an $[N(n_c+1)^2+1] \times [N(n_c+1)^2+1]$ linear system of equations for the unknown multipole moments. In the present simulation, we include only the $n = 0$ and $n = 1$ terms in the expansion. The $n = 0$ term is the classical monopole term (referred to as M). The $n = 1$ terms are the dipole terms (referred to as D) in the spherical harmonics expansion. Although these dipole terms lead to a nonuniform concentration gradient along the surface of the particle, the particle will still remain spherical. However, the center of the particle will move with a velocity given by Eq. (2.48). If terms greater than $n = 1$ are included, the particle will change its shape from a sphere. Thus, the inclusion of these higher order terms is inconsistent with our earlier assumption that the particles are spherical and we shall therefore only include monopole and dipole terms in our description of the diffusion field.

In principle, all the particles in the system interact with each other, and thus the linear system of equations for the multipole moments is extremely large. However, the interaction between particles at large distances of separation is negligible, since the interparticle interactions are screened out. This, in turn, greatly reduces the size of the linear system which needs to be solved to determine the multipole moments. The screening is due to the mass conservation constraint. To illustrate, for the monopole approximation, the growth rate of a particle is given by the summation of the growth rates of the other particles divided by the separation distance, as shown in Eq. (2.42) with $n = 0$. Thus, the effect of other particles on the growth rate of an individual particle decreases as the inverse of the separation distance. However, the number of particles in a spherical shell at that separation distance increases as the square of the separation distance. This suggests that the interaction between particles at large distances of separation increases linearly with the distance from a particle. However, since the summation of the growth rates for the entire system is zero, the summation of the growth rates of particles in a spherical shell at a large distance from a particle is expected to approach zero because the number of particles in that shell becomes large. Thus, the interaction of a particle with others at large distances becomes smaller as the distance increases. The growth rate of a given particle, considering only the particles within a certain distance, the cutoff distance, is expected to approach an asymptotic value as this cutoff distance increases. Figure 1 shows the growth rate of a particle where only those particles within a spherical region of radius equal to the cutoff distance from a particle, x_c, have been considered at a volume fraction of 0.1. It is clear that the growth rate of the particle approaches a constant as the cutoff distance increases. To obtain a 1% accuracy in the growth rate of a particle, compared to its asymptotic value, within the monopole approximation about 130, 120, 100, and 80 particles have to be included within the cutoff distance for volume fractions of 0.05, 0.1, 0.2, and 0.3, respectively, and using the monopole plus dipole approximation about 60, 50, and 30 particles are necessary for volume fractions of 0.1, 0.2, and 0.3, respectively. The above numbers are estimates found by examining the growth rates of large particles. For small particles, which have growth rates less than approximately -0.5, the growth rate converges much faster

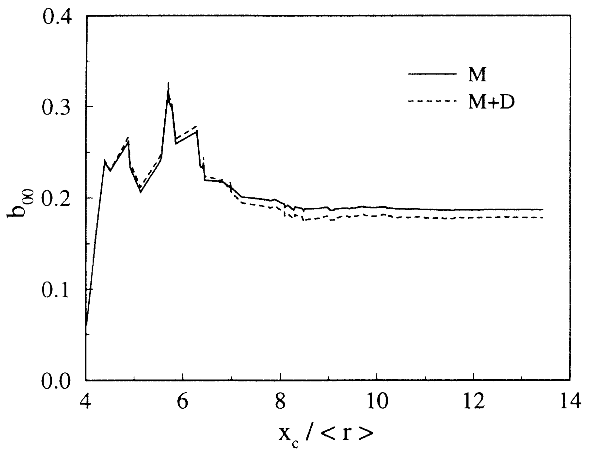

FIG. 1. The growth rate of a particle as a function of the cutoff distance, x_c, relative to the average radius $\langle r \rangle$ at a volume fraction of 0.1.

as the cutoff distance increases than that for large particles. This is because the effects of the other particles become small as the radius of a particle becomes small. Multiplying Eq. (2.42) by r_i and rewriting,

$$b_{00}^{i} = (u_{00} r_i - 1) - r_i \sum_{j \neq i}^{N} \sum_{nm} \frac{(-1)^n r_j^n}{d_{ij}^{n+1}} \frac{1}{(2n+1)} Y_n^m(\mathbf{d}_{ij}) b_{mn}^{j}. \quad (3.1)$$

When r_i approaches 0, b_{00}^{i} becomes -1 regardless of the order of the multipole moment kept in the solution to the diffusion field. For small particles, the term $u_{00} r_i - 1$ is dominant due to a factor r_i before the summations. Interestingly, the convergence rate of the particle growth rate using the monopole plus dipole approximation is generally faster than that of the monopole approximation. In addition, the convergence rates of the dipole moments are the same as that of the growth rate.

The simulations were performed at volume fractions of 0.05, 0.1, 0.2, and 0.3. At a volume fraction of 0.05 only the monopole approximation was employed, since the dipole contributions are expected to be small. At volume fractions of 0.05, 0.2, and 0.3, the particles were placed at random locations within a box, but with no particle overlap. This method of placement is denoted by $d = 0$. At a volume fraction of 0.1 two different methods were used to place particles in the box. The first method was identical to that used at the other volume fractions. The second method was to place the particles at random within the box, except that a small spherical shell, or depletion zone, surrounding each particle was created wherein particles could not be placed. In this case the thickness of the shell or size of the depletion zone was chosen to be 0.5 times the radius of a particle, and hence these calculations will be denoted by $d = 0.5$. In the Rikvold and Gunton model [28], the depletion zone is given by $\phi^{-1/3} - 1$, where ϕ is the volume fraction of particles. At a volume fraction of 0.1 the depletion zone is then given by 1.15. However, if a depletion zone higher than 0.6 is employed, it is very difficult to successfully place the particles in the box, and thus we limited the depletion zone size to 0.5. In two-phase systems created by a nucleation and growth process, for example, the initial spatial distribution of particles is related to the spatial distribution of nucleation sites, and thus may be different from either of the two initial spatial distributions we employed. Nevertheless, if the long-time state of the system can be made time independent under the scaling of the average particle radius, then any initial spatial distribution of particles should evolve to a unique scaled form.

In order to access the long-time behavior of the system, we employed 20 000 particles at the beginning of the simulations. Calculations at a volume fraction of 0.1 were also performed with 50 000 particles to ensure that 20 000 particles were sufficient to allow the system to approach a scaled time independent state. The procedure of each simulation is as follows,

1. 20 000 particles which satisfy the particle size distribution function found near the end of a previous run are placed at random locations, with or without depletion zones, in a box. The box is repeated periodically to fill all space.
2. The growth rates and the migration rates of the particles are calculated.
3. The particle volume and location are updated using the simple explicit Euler method.
4. Procedures 2 and 3 are repeated until the number of particles reaches 100.

The radius and the location of the particles are stored every 30 time steps. The cutoff distances using the monopole approximation are chosen to be 15, 10.5, 7.5, and 6.3 times the average particle radius for volume fractions of 0.05, 0.1, 0.2, and 0.3, respectively. The cutoff distances using the monopole plus dipole approximation are 9, 6.4, and 5.3 for volume fractions of 0.1, 0.2, and 0.3, respectively. It is expected that $\langle r \rangle^3$, where $\langle r \rangle$ is the average particle radius, is proportional to time so that the time step Δ can be given by $\Delta = C_{ts} \langle r \rangle^3$ where C_{ts} is a constant. This method causes the volume fraction to increase during the simulations, so that the value of C_{ts} has to be chosen carefully. This increase in the volume fraction is because the volume of a particle can become negative over a time step, since the volume change of each particle is calculated by multiplying its growth rate by Δ. Thus, more mass is transferred from this shrinking particle to the other particles in the system than should be possible based upon the actual volume of this particle. In these simulations, C_{ts} is chosen to be 0.01 for the monopole approximation and 0.0067 for the monopole plus dipole approximation. Particles smaller than $0.1 \langle r \rangle$ are removed from the system before calculating the growth rates to decrease the change in the volume fraction. Using this procedure the volume fraction change was typically 5%. Simulations with a smaller time step, $C_{ts} = 0.0033$, at a volume fraction of 0.1 were also performed. In this case the volume fraction change was less than 0.05%, and produced the same results as the simulation using $C_{ts} = 0.01$.

Once the form of the scaled time independent particle size distribution was determined at a particular volume fraction, this distribution was used as the initial size distribution for a number of runs with different initial random spatial distributions of the particles. For the monopole approximation, four runs were performed at a volume fraction of 0.05 and eight runs were performed at the other volume fractions. Also, four runs were performed with initial depletion zones at a volume fraction of 0.1. Finally, two runs with 50 000 particles were performed with and without depletion zones at a volume fraction of 0.1. For the monopole plus dipole approximation, three runs were performed at each volume fraction. Unless otherwise mentioned, the results presented have been averaged over the previously mentioned number of independent runs.

As pointed out by Beenakker [15], particle overlaps are frequently found during the simulations. It is nearly impossible to avoid some degree of particle overlap, since the particles in the simulations are not permitted to change their shape. If the higher order multipole moments are included in the description of the diffusion field, and thus the particles can change their shape, overlaps are not observed [37,41,42]. The effects of particle overlap can be illustrated by considering the expression for the growth rate of a particle in a two particle system using the monopole approximation,

$$b_{00}^{1} = \frac{r_1 - r_2}{r_1 + r_2 - 2r_1 r_2/d}. \tag{3.2}$$

Thus, if $d = 2r_1r_2/(r_1 + r_2)$, b_{00}^1 is singular and changes sign for d less than this value. A similar result can be obtained for the monopole plus dipole approximation. In contrast, if all the terms in the multipole expansion are included, the growth rate becomes singular at the contact distance, $d = r_1 + r_2$. Since the growth rate changes continuously for small overlaps using either the monopole or monopole plus dipole approximation, the effects of overlap are usually neglected. However, in some cases this overlap introduces major errors in the calculations. For example, at a volume fraction of 0.4, within the monopole plus dipole approximation, the magnitude of the particle overlaps was sufficiently large to cause a very large change in the volume fraction of the particles and the particle size distribution to have a long tail at large radius. Table I shows the fraction of the overlapping particles and the average over all the overlapping particles of the overlap length divided by the radius of the particle near the end of the simulations. At a volume fraction of 0.05 the fraction of the overlapping particles is very small. As volume fraction increases the fraction and the magnitude of the overlap increases. However, if the dipole terms are included, the fraction and magnitude of the overlap decreases significantly. This is due to particle migration. Although at a volume fraction of 0.3, in the monopole approximation, the overlap length divided by the radius of the particle can be as large as 0.8, it is difficult to find a particle where the overlap was sufficient to cause the particle growth rate to become singular. Clearly, there may be a large error in the growth rate of this particular particle which has a relative overlap of 0.8. However, the fraction of particles with such a large overlap is not large. Thus, although these overlaps introduce significant error in the spatial distribution functions, the error introduced in the temporal behavior of the system is unclear.

TABLE I. Fraction of the overlapping particles and average over all the overlapping particles of the overlap length divided by the particle radius for various volume fractions near the end of the simulations.

Volume fraction		Fraction	Average overlap
0.05	M	0.002	0.10
0.1	M	0.026	0.12
	$M+D$	0.005	0.025
0.2	M	0.22	0.14
	$M+D$	0.054	0.061
0.3	M	0.72	0.16
	$M+D$	0.28	0.074

IV. RESULTS AND DISCUSSION

A. Particle migration

The inclusion of multipole moments beyond a monopole in the description of the diffusion field implies that the centers of mass of particles will not remain fixed in space. The particle migration is a result of the nonuniform concentration gradient over the surface of the particle. This particle migration can be significant. Figure 2 shows the radius and location of the center of a particle, scaled by the initial average particle radius $\langle r_0 \rangle$ as a function of time at a volume fraction of 0.1. The initial location of the center of the particle is chosen as the origin. At the beginning of the calculation, this particle grows with time as most of the particles in the system are smaller than this particle. However, as the average particle radius increases with time this particle eventually shrinks for $t > 50$. The total migration distance of this particle is about $1.3\langle r_0 \rangle$, or slightly more than the initial radius of the particle. At early times, $t < 10$, the trajectory of the particle is quite convoluted, reflecting the changing local environment of this particular particle. Thus, dur-

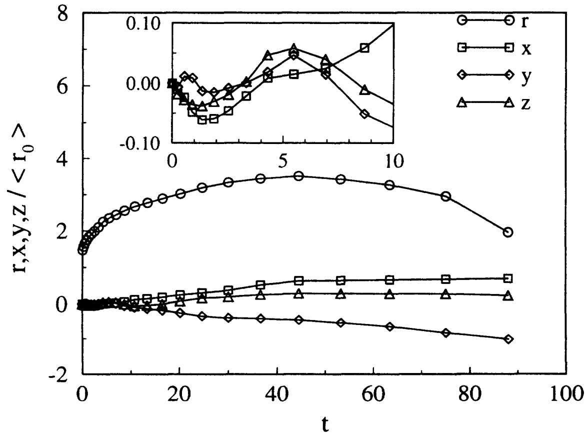

FIG. 2. The radius r and location of a particle, in terms of the Cartesian coordinates x, y, z, as a function of time at a volume fraction of 0.1.

ing coarsening, both the sizes of the particles *and* their locations change with time. This is also the major reason why the fraction of overlapping particles decreases with the addition of dipole terms in the description of the diffusion field (see Table I). In an effort to assess the importance of these particle migrations, simulations were performed at a volume fraction of 0.3 using the monopole plus dipole approximation but not allowing the particles to migrate. In this case the volume fraction shift was very large due to the large magnitude and fraction of the particle overlap. This large shift in the volume fraction is a result of including dipole terms without allowing the particles to migrate, and thus the description of the diffusion field was not self-consistent. Thus, we can speculate that if the higher order terms beyond the dipole terms are included to calculate the growth rates, the particles must change shape to be self-consistent and avoid large errors.

B. Radial distribution and pair correlation functions

Here we examine the development of spatial correlations in real space. We define the radial distribution function as a ratio of the number of particles whose centers lie within the spherical shell of radius x and thickness dx surrounding a particle, to the number of particles in the shell expected from the number density of the system,

$$G(x) = \frac{\text{[No. of particles in the spherical shell (observed)]}}{\text{[No. of particles in the spherical shell (from density)]}}. \tag{4.1}$$

The radial distribution function is expected to approach 1 as x increases and is zero in the limit $x \to 0$. Our interest is in the shape of the radial distribution function at intermediate distances. If the system is in the scaling region, when the radial distribution function is scaled by the average radius, it must be time independent. The radial distribution function defined in Eq. (4.1) depends only on the radius of the shell and the effect of particle radius is ignored.

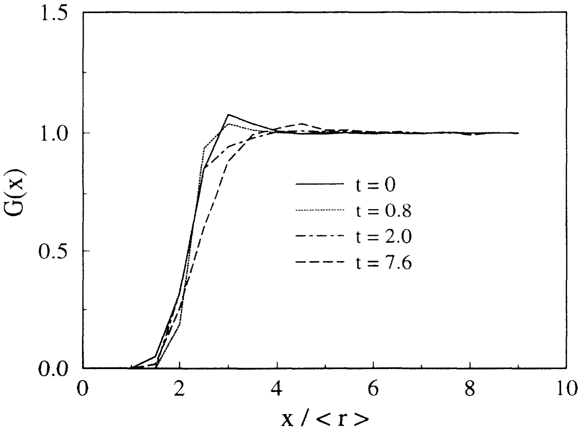

FIG. 3. Time evolution of the radial distribution function without initial depletion zones ($d = 0$) at a volume fraction of 0.1 using the monopole approximation.

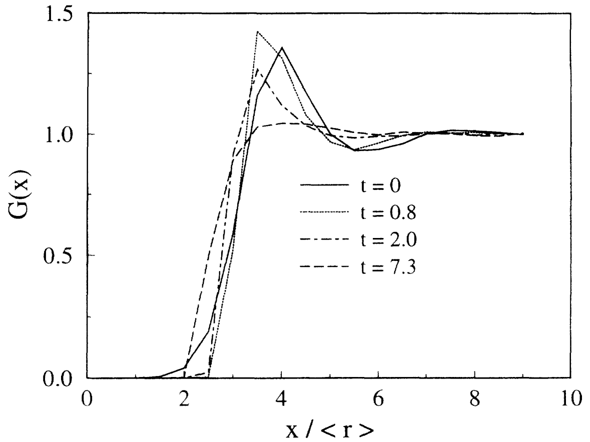

FIG. 4. Time evolution of the radial distribution function with initial depletion zones ($d = 0.5$) at a volume fraction of 0.1 using the monopole approximation.

Figure 3 shows the time evolution of the radial distribution function scaled by the average particle radius without the initial depletion zones ($d = 0.0$) at a volume fraction of 0.1 using monopole approximation. There is a small peak at about $x/\ \langle r \rangle = 3$ at $t = 0$. This is a natural feature of the radial distribution function for a randomly distributed polydisperse system [43]. Generally $G(x)$ approaches 1 in an oscillatory manner with increasing $x/\langle r \rangle$. The peak position shifts to the larger x as time increases and the peak height decreases at the beginning but increases at intermediate times. Figure 4 shows the time evolution of the radial distribution function at a volume fraction of 0.1 beginning with a spatial distribution produced using depletion zones ($d = 0.5$) and the monopole approximation. There is a large peak at about $x/\langle r \rangle = 4$ at $t = 0$ and oscillations in the radial distribution function at larger x are more apparent. The peak position shifts to smaller $x/\langle r \rangle$ as time increases, opposite to the direction when beginning with a random distribution without depletion zones (see Fig. 3), and the peak height increases at the beginning but decreases at intermediate times. Figure 5 shows the radial distribution function near the end of the simulations. The initial radial distribution functions, $d = 0$ and $d = 0.5$, are also shown in Fig. 5. As will be mentioned later, the scaled particle size distribution is time independent within the scatter of the data during the simulations, so that the temporal evolution of the radial distribution function is not due to significant changes in the scaled particle size distribution. The radial distribution function changes drastically at early times, but the changes become slower as time increases, with the radial distribution function becoming time independent, within our resolution, after about $t = 25$. At this time the number of particles in the system is about 1000, corresponding to about 5% of the initial number of particles. The results shown in Fig. 5 are an average of twelve different times corresponding to 1000–100 particles over the noted range in time. It

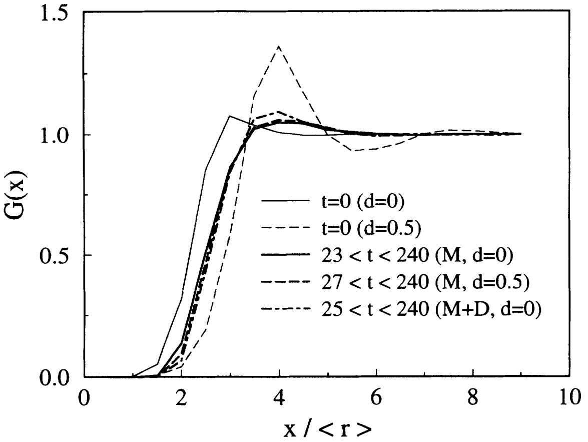

FIG. 5. The radial distribution functions in the late stage at a volume fraction of 0.1, along with the initial radial distribution functions.

should be emphasized that the radial distribution functions produced using either an initial depletion zone or no depletion zone yield nearly the same radial distribution function near the end of the simulations. The long-time results fall between the two initial radial distribution functions. In addition, the similarity of the results shows that starting with 50 000 particles or 20 000 particles has no effect on the results. Thus, it appears that the system chooses a unique scaled time independent spatial distribution of particles. The radial distribution function in the late stage using the monopole plus dipole approximation, $d = 0$, is also shown in Fig. 5. At this volume fraction, the differences between the two approximations are small.

Figure 6 shows the radial distribution functions at various volume fractions. The solid lines are the results near the end of the simulations using the monopole plus dipole approximation. The results using the monopole approximation are shown at a volume fraction of 0.05. The broken lines are the initial radial distribution functions of a random spatial distribution without depletion zones. Generally, the number density of particles near a particle is less than that of the random distribution and the peak positions shift to larger distances. As volume fraction increases, the differences between the time independent radial distribution function and the initial random distribution decreases. Although the differences between the time independent radial distribution function and the initial random distribution at a volume fraction of 0.3 are small, this does not mean that the particle spatial correlations in the late stage are close to those of a random distribution. This will be shown by examining the pair correlation functions.

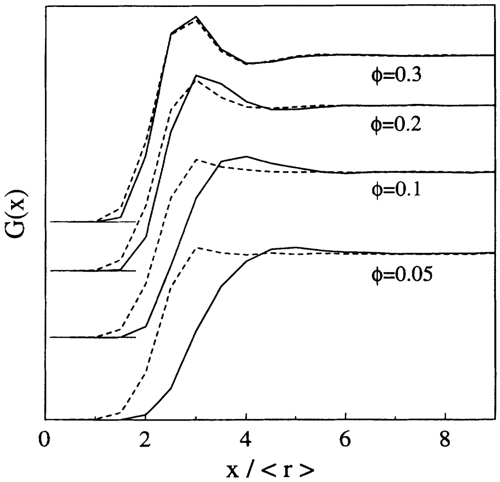

FIG. 6. The radial distribution functions at various volume fractions. The solid lines are the results in the late stage. The broken lines are the initial radial distribution functions with $d = 0$.

Since the effect of particle size is not considered in the radial distribution function, we introduce a pair correlation function $G(r, r', x)$. The pair correlation function is defined as the number of particles of radius r' whose centers lie within the spherical shell of radius x and thickness dx surrounding a particle of radius r divided by that expected from the number density of particles of size r' in the system. $G(r, r', x)$ approaches 1 as x goes to infinity and is zero when $x < r + r'$. Note that $G(r, r', x)$ and $G(r', r, x)$ are identical. Although the pair correlation function is defined for every pair of r's, the number of particles in the system is not large enough to investigate all possible pairs. Thus the particles are divided into three classes, smaller than $0.75\langle r\rangle$, between $0.75\langle r\rangle$ and $1.25\langle r\rangle$, and larger than $1.25\langle r\rangle$; we will refer to each size range as small, medium, and large, respectively.

Figures 7–10 show the small-small, small-medium, small-large, and large-large correlation functions, respectively, at $t = 0$ and near the end of the simulations at a volume fraction of 0.1. The late stage results shown in these figures are an average of twelve different times, in the same manner as was done for the radial distribution functions shown in Fig. 5. An important feature evident in the small-small correlation function shown in Fig. 7 is that near the end of the simulation a large depletion

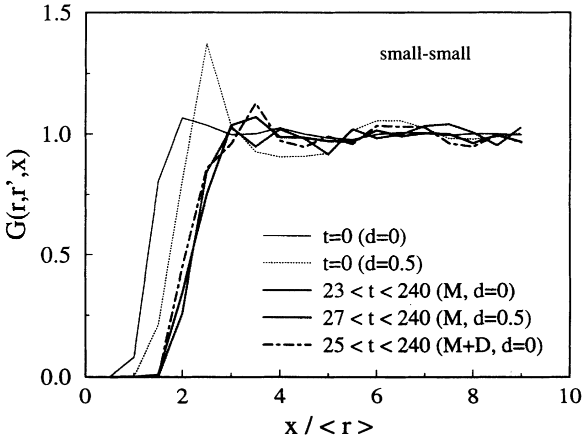

FIG. 7. The small-small correlation function at a volume fraction of 0.1. The initial and late-stage correlation functions are shown. The correlation functions in the late stage were computed using either the monopole or monopole plus dipole approximation.

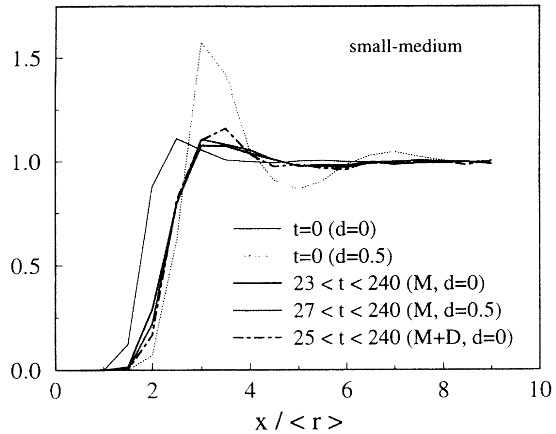

FIG. 8. The initial and late-stage small-medium correlation function at a volume fraction of 0.1.

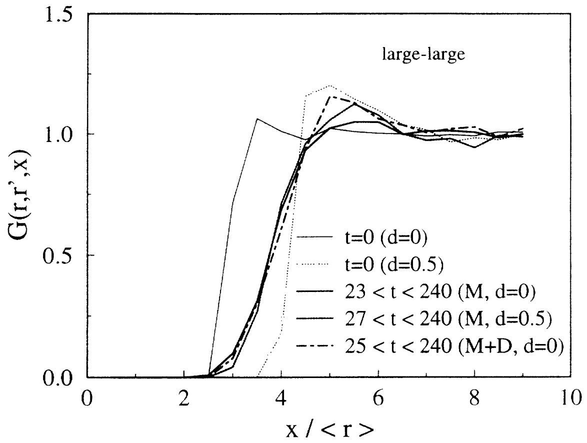

FIG. 10. The initial and late-stage large-large correlation function at a volume fraction of 0.1.

zone with a width of $x/\langle r\rangle = 1.5$ is present. This is larger than the depletion zone of the initial spatial distribution using $d = 0.5$. Also, the peak in the long-time correlation function, which is large in the initial distribution of $d = 0.5$, is not apparent. Similar trends can be observed in the small-medium correlation function, Fig. 8. Although a depletion zone exists for small-medium particles, the size of the depletion zone is now only as large as that of the initial spatial distribution with d=0.5. Also, a small peak in the correlation function is apparent in this case. Although the positions of the peaks in the small-medium correlation function are the same as that of the initial spatial distribution with $d = 0.5$, the heights of the peaks are much lower. Finally, the large oscillations in the initial small-medium correlation function produced using $d = 0.5$ are not apparent in the late-time results. As shown in the small-large correlation function for $d = 0$ using the monopole approximation, Fig. 9, for still larger particle sizes, there is no depletion zone. In this case, the density of particles gradually goes to zero at small $x/\langle r\rangle$, finally becoming zero where the initial density of particles with $d = 0$ is zero. As the particles were placed at random locations, but without overlaps for $d = 0$, the point at which $G(r, r', x)$ is zero is approximately the lower limit for the value of $x/\langle r\rangle$ at which the particle density can be nonzero. This can be clearly observed in the large-large correlation function, Fig. 10. In both of these cases the late-time results fall between the two initial correlation functions. The medium-medium and medium-large correlation functions are similar to those of the large-large correlation function [39]. The correlation functions produced using the monopole plus dipole approximation are also shown in Figs. 7–10. The results show similar trends, although the peak heights are slightly higher than those found with the monopole approximation. In general, except for the small-small correlation functions, the number density of the particles at small $x/\langle r\rangle$ is less than that produced using no depletion zones, $d = 0.0$, but higher than that produced using a depletion zone of $d = 0.5$.

Although the scaled time independent spatial correlation functions found at a volume fraction of 0.1 for the monopole and monopole plus dipole approximations are nearly identical, this is not the case at a volume fraction of 0.3 (see Fig. 11). For example, the large-large corre-

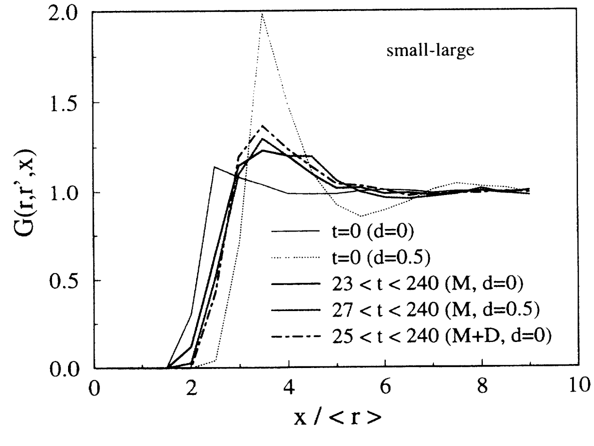

FIG. 9. The initial and late-stage small-large correlation function at a volume fraction of 0.1.

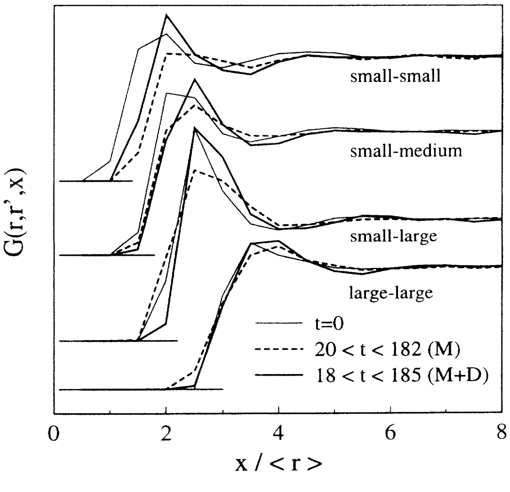

FIG. 11. The initial and late-stage pair correlation functions at a volume fraction of 0.3.

lation function found using the monopole approximation has an extended tail at small distances. This tail implies that a nonzero density of large particles will exist surrounding another large particle at distances below that of the random $d = 0$ initial spatial distribution. In addition, as shown in Table I, the fraction of overlapping particles using the monopole approximation is much larger than that found using the monopole plus dipole approximation at this volume fraction. Thus, the tail at small distances found using the monopole approximation may be due to extensive particle overlaps. At a volume fraction of 0.2, this same problem with the monopole approximation is present; however, the differences between the scaled spatial correlation functions using the two approximations are not as large as those at a volume fraction of 0.3. Therefore, the monopole approximation gives a poor representation of the diffusion field in a system undergoing coarsening at volume fractions higher than approximately 0.1. At a volume fraction of 0.3, the large-large correlation function using the monopole plus dipole approximation shows a very small tail at small distances. This suggests that the effects of changes in particle shape will be important in systems with volume fractions in excess of 0.3.

In contrast to the similarity in the initial and late-time radial distribution functions at a volume fraction of 0.3, clear differences exist between the initial and late-time correlation functions. Specifically, a depletion zone is present in the small-small correlation function and a depletion zone is not present in the small-medium, small-large, and large-large correlation functions. In addition, the number density of particles near a particle is less than that of the initial random distribution for the small-medium and small-large correlation functions. For the large-large correlation function, the differences between the initial and late-stage scaled correlation functions are small. One reason for this may be that the dense packing of particles at this volume fraction will not allow the large particles to assume a spatial distribution which is much different from that of a random spatial distribution. Thus, the trends in the dependence of the spatial correlation functions on particle radius observed at a volume fraction of 0.1 are also evident at a volume fraction of 0.3.

A general conclusion which can be drawn from these results is that the size of the depletion zone surrounding a particle is a function of particle size. A depletion zone exists in the small-small correlation functions because the majority of these particles are shrinking, and thus the spacing between the interfaces of these small particles increases as they shrink to zero size, even if they happened to be near one another. In contrast, as most large particles are growing, if two of these growing particles are located near one another the distance between the interfaces of these particles can decrease with time. This would happen if the two particles are approximately the same size, so that the tendency of one particle growing at the expense of the other is small, and if these particles are surrounded by smaller particles. Thus, the two particles grow at the expense of the surrounding smaller particles, instead of one another, and their interfaces can almost touch. Eventually, however, the size difference between these large particles becomes important, and one grows at the expense of the other. This process must be fairly rare, for it depends on two large particles of nearly the same size being located near each other. The rarity of this occurrence is likely the reason why there is only a small, but nonzero, probability of finding large and medium particles near each other at very small distances of separation.

It has been suggested that small particles tend to be preferentially located near the large particles [17] since very large particles always grow, resulting in the particles in their vicinity being small. In addition, experiments in a two-dimensional system [31] show a strong peak in the small-large correlation function. As shown in Figs. 9 and 11, the small-large correlation functions also show similar peaks. However, one must be careful in interpreting such results. At a volume fraction of 0.1, the small-large correlation function does show a higher peak than that of an initial distribution without depletion zones, but a much lower peak than that when the particles are placed in the system with a depletion zone. In addition, the probability of finding a small particle near a large particle at small distances of separation, $x/\langle r \rangle \leq 3$, is *smaller* than that of an initial random distribution without depletion zones. This is because small particles which are located near large particles disappear rapidly, due to the large concentration gradient that exists between the two particles. Thus, at a volume fraction of 0.1, depending on the distance, the probability of finding a small particle near a large one can be either greater than or less than that of a random distribution. At a volume fraction of 0.3, the peak heights in the small-large correlation functions for both the initial random and late-time spatial distribution are nearly the same. However, at smaller distances, there are fewer smaller particles near large particles than would be expected from an initial random distribution (see the more accurate $M + D$ curve). Thus, we find that at both high and low volume fractions, strong local diffusional interactions induce the density of smaller particles near large particles to be lower than that of a random distribution without depletion zones.

Attempts have been made to determine the particle size distribution from the measured structure function using the Percus-Yevick hard sphere model with depletion zones [29,30]. In this spirit, we tried to reproduce the late-time spatial correlation functions using a depletion zone model for various values of d. As might be expected from examining Figs. 7–11, a simple depletion zone model was incapable of reproducing the late-time correlation functions. This may be one reason why the particle size distributions determined from scattering measurements are much different from those predicted by theory.

C. The structure function

Particle spatial correlations are also characterized by the structure function. The structure function is defined as a spherically averaged Fourier transform of the concentration field,

$$S(k,t) = \frac{\int S(\mathbf{k},t)d\Omega_k}{\int d\Omega_k}$$

$$= \left\langle \left| \frac{1}{V} \int_V \mathcal{U}(\mathbf{x}) \exp(i\mathbf{k}\cdot\mathbf{x})d\mathbf{x} \right|^2 \right\rangle_\Omega , \qquad (4.2)$$

where Ω_k is the solid angle in k space, $|\cdots|$ denotes the magnitude of a complex quantity,

$$\mathcal{U}(\mathbf{x}) = u(\mathbf{x}) - \langle u \rangle, \qquad (4.3)$$

$\langle u \rangle$ is the volume averaged concentration, and $\langle\cdots\rangle_\Omega$ in Eq. (4.2) is defined as the spherical average. We shall assume that the concentration in the particles and in the matrix are given by constants $\mathcal{U}_p$ and $\mathcal{U}_m$, respectively. In reality, the concentration is not constant both in the particles and in the matrix, but the variations in the concentration in both phases are much smaller compared with the difference between $\mathcal{U}_p$ and $\mathcal{U}_m$. Although both $\mathcal{U}_p$ and $\mathcal{U}_m$ depend on the system under consideration and experimental conditions, different values of $\mathcal{U}_p$ and $\mathcal{U}_m$ only result in a change in the constant factor in Eq. (4.2). Since our interest is the shape of the structure function and not its magnitude, we shall choose $\mathcal{U}_p$ and $\mathcal{U}_m$ to be 1 and 0, respectively, for simplicity. Using the periodic boundary conditions, and the spherical morphology of each particle, Eq. (4.2) becomes,

$$S(k,t) = \left\langle \left| \sum_j^N \frac{4}{3}\pi r_j^3 \Psi(kr_j) \exp(i\mathbf{k}\cdot\mathbf{d}_j) \right|^2 \right\rangle_\Omega$$

$$= \left\langle \sum_j^N \sum_{j'}^N \frac{4}{3}\pi r_j^3 \frac{4}{3}\pi r_{j'}^3 \Psi(kr_j)\Psi(kr_{j'}) \times \exp(i\mathbf{k}\cdot\mathbf{d}_{jj'}) \right\rangle_\Omega , \qquad (4.4)$$

where N is the number of particles in the unit cell, $\mathbf{d}_j$ is a position vector of the center of particle j, and $\Psi(kr_j)$ is the form factor of a sphere,

$$\Psi(kr_j) = 3\frac{\sin(kr_j) - kr_j\cos(kr_j)}{(kr_j)^3}. \qquad (4.5)$$

The structure function was calculated using Eq. (4.4). Taking the spherical average in Eq. (4.4) yields the spherically averaged structure function for a polydisperse system of spherical particles,

$$S(k,t) = \sum_j^N \left[\frac{4}{3}\pi r_j^3 \Psi(kr_j)\right]^2 + \sum_j^N \sum_{j'\neq j}^N \frac{4}{3}\pi r_j^3 \frac{4}{3}\pi r_{j'}^3 \times \Psi(kr_j)\Psi(kr_{j'})\frac{\sin(kd_{jj'})}{kd_{jj'}}. \qquad (4.6)$$

The first term in Eq. (4.6) represents the scattering intensity from the individual particles. The second term represents the interference between the particles and is related to the pair correlation function through the double summation. If the system is in the scaling region, $S(k,t)$ obeys the scaling law,

$$S(k,t) = \langle r(t) \rangle^3 s(q), \qquad (4.7)$$

where $q = k\langle r(t) \rangle$ and $s(q)$ is the scaled time independent structure function.

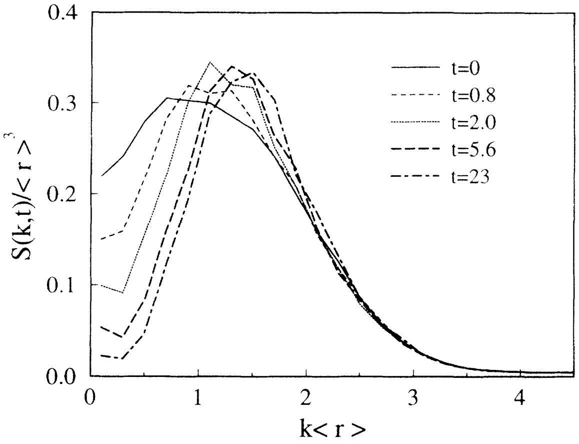

FIG. 12. Time evolution of the scaled structure function using the monopole approximation when the particles were placed initially at random locations with no depletion zones ($d = 0$) at a volume fraction of 0.1.

Figure 12 shows the time evolution of the structure function, scaled by the cube of the average particle radius using the monopole approximation, for a system where the particles are placed randomly in the system with no depletion zones ($d = 0$) at a volume fraction of 0.1. The position of the peak increases with time and the peak height increases initially and then appears to decrease at intermediate times. The value of the structure function at small $k\langle r \rangle$ decreases drastically as time increases. Figure 13 shows the time evolution of the scaled structure function using the monopole approximation where the

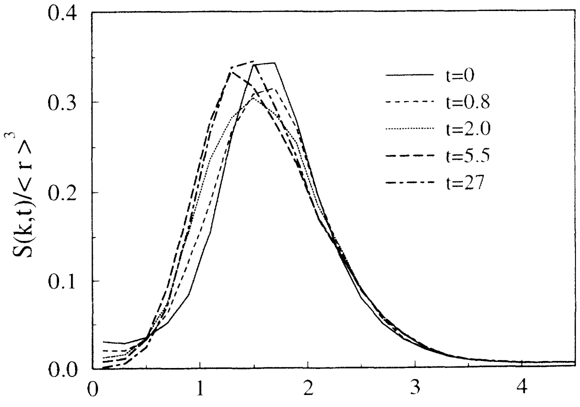

FIG. 13. Time evolution of the scaled structure function using the monopole approximation when the particles were placed initially at random locations with depletion zones ($d = 0.5$) at a volume fraction of 0.1.

particles are placed in the system at random using depletion zones ($d = 0.5$) at a volume fraction of 0.1. The peak position moves to smaller $k\langle r\rangle$ as time increases and the peak height decreases initially but increases in the intermediate stage. It is clear that mixtures created by placing particles at random using a depletion zone produces a better approximation to the scaled time independent structure function than placing particles in the system without depletion zones. However, the temporal evolution of the scaled structure function beginning with depletion zones is evident. Therefore, as our real space correlation functions indicate, the depletion zone model does not reproduce the proper spatial correlations. Since the scaled particle size distributions did not change, to within the resolution of our data, during these calculations, the changes in the structure functions observed in Figures 12 and 13 are due solely to the development of particle spatial correlations. Figs. 14 and 15 show the scaled time independent structure functions, $s(q)$, in the late stage at volume fractions of 0.1 and 0.3, respectively. The scaled structure functions become time independent in the late stage, as expected. At a volume fraction of 0.1, Fig. 14, all of the results agree reasonably well. However, at a volume fraction of 0.3, Fig. 15, the differences between the structure functions using the monopole and monopole plus dipole approximations are not small. This difference is consistent with the difference in the pair correlation functions found using the monopole and monopole plus dipole approximations shown in Fig. 11. The arrows in the figures denote the location of a secondary maximum in the structure function which will be discussed later. Yao *et al.* [7] calculated the structure function using a system which initially had 1000 particles. The scaled structure functions they obtained during coarsening for systems containing 500, 400, and 300 particles are not time independent. Since their results appear to correspond to times in the range 1–3 in the present simulations, it is likely that the scaled spatial correlations in their calculations have not reached their time independent form.

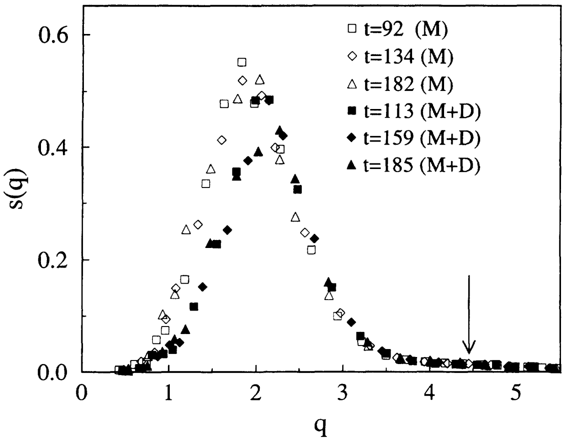

FIG. 15. The scaled time independent structure function in the late stage using the monopole and monopole plus dipole approximations at a volume fraction of 0.3.

The asymptotic behavior of the structure function at small and large wave numbers has been investigated theoretically. For large wave numbers, the structure function has the asymptotic form of $s(q) \sim q^{-4}$ known as Porod's law [44]. This is a result of the sharp interface between the particle and matrix. For small wave numbers, the asymptotic behavior of $s(q) \sim q^4$ has been proposed for systems undergoing coarsening [33] and spinodal decomposition [45–49]. This asymptotic dependence is due to the presence of a certain form of the particle spatial correlations. It is difficult to determine $s(q)$ in these limits experimentally because the scattering intensity is very small at small and large q. Figure 16 shows a log-log plot of the scaled structure function in the late stage. The solid lines in the figure indicate slopes of 4 and -4, respectively. As mentioned earlier, the radial distribution function becomes time independent, to within the scatter in the data, when the number of particles becomes less than about 1000, or $t > 25$. The structure function except at several of the smallest wave numbers becomes time independent at this point as well. The structure function at the very lowest wave numbers appears to systematically decrease as time increases, despite the nearly time independent correlation functions, when the num-

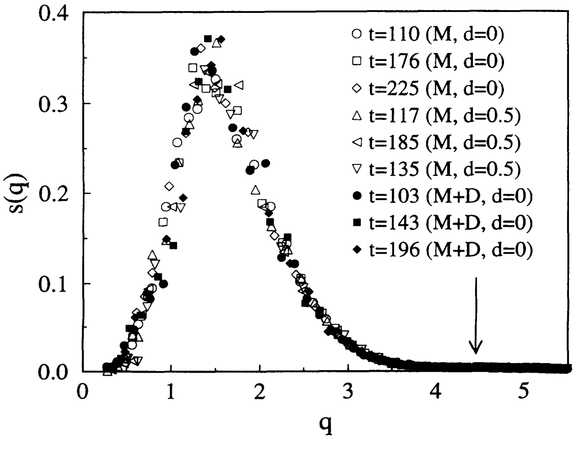

FIG. 14. The scaled time independent structure function in the late stage using the monopole and monopole plus dipole approximations at a volume fraction of 0.1.

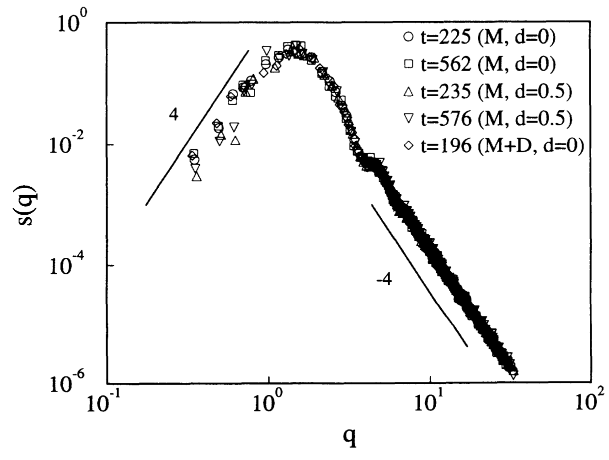

FIG. 16. A log-log plot of the scaled structure function at a volume fraction of 0.1 at various times calculated using both the monopole and monopole plus dipole approximations.

ber of particles is below 1000. However, the magnitude of this change is quite small and can only be observed in a log-log plot, such as Fig. 16. Nevertheless, the structure function becomes time independent, to within the scatter of the data, even when viewed on a log-log plot, when the number of particles is less than about 300, or $t > 100$, corresponding to about 1.5% of the initial number of particles. The results at longer times using the simulations beginning with 50 000 particles, are also shown in the figure. There is no significant difference between the results with systems beginning with 20 000 or 50 000 particles. The slopes of the structure function as a function of q seems to approach 4 for small q. However, it is difficult to determine accurately the asymptotic behavior of $s(q)$ at small wave numbers, since the largest wavelength is restricted to the size of the computational cell. Although our data have a slope which is nearly 4, at least one order of magnitude smaller range of wave numbers is necessary to establish accurately the slope of the structure function at small wave numbers. Unfortunately, this will require systems which have approximately 1000 times more particles than those used in these calculations.

As mentioned above, at large q the structure function decays as q^{-4}. However, it is also evident from Fig. 16 that at large q oscillations about this q^{-4} decay are present. In Figs. 14 and 15, the position of one of these oscillations is indicated by the arrow; however, the amplitude of the oscillation is quite small. The existence of these oscillations becomes apparent in a log-log plot of $s(q)$ vs q. A log-log plot of the time dependent structure functions shown in Figs. 12 and 13 also shows these oscillations. In this case, the positions and amplitudes of the oscillations do not depend on time, while the small wave number portion of the structure function is time dependent. For $q > 3.5$ the scaled structure function was time independent. This is also the case for both time dependent and independent structure functions found at the other volume fractions.

The origin of the oscillations follows from an analysis of the long wave number limit of the structure function. Specifically, for sufficiently large wave numbers the second term in Eq. (4.6), which is related to the spatial arrangement of the particles, is small compared to the first term. Thus, in the large wave number limit the structure function is approximately given by

$$S(k,t) \simeq \sum_{j}^{N} \left[\frac{4}{3} \pi r_j^3 \Psi(k r_j) \right]^2 . \tag{4.8}$$

Figure 17 shows the structure function at large wave numbers at volume fractions of 0.1 and 0.3. The solid lines are calculated using Eq. (4.8). For $q > 3.5$ the data points and the solid lines agree well. This suggests that the oscillations are simply due to the spherical shape of the particles and the particle size distribution. This is also consistent with the observation that the scaled structure function was time independent for $q > 3.5$ even when the scaled structure function at small q was evolving in time, since the scaled particle size distribution was time independent during the simulation. At a volume fraction of 0.1, the solid line agrees well with the data points almost all the way to the main peak of the structure function. However, this does not mean that the interference term is not important near the main peak.

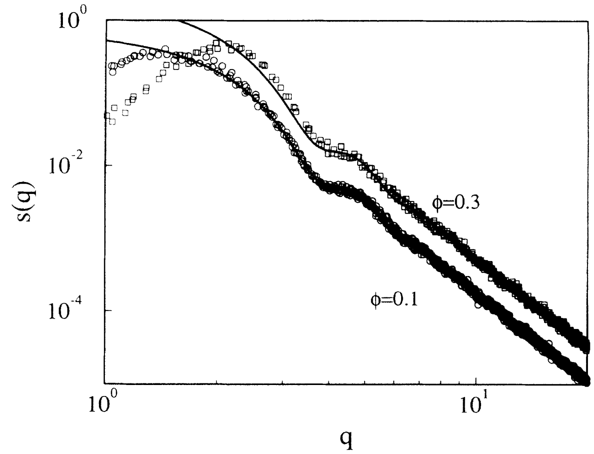

FIG. 17. The large wave number behavior of the structure function at volume fractions of 0.1 and 0.3.

The existence of the oscillations in the large wave number portion of the structure function has been suggested by Fratzl *et al.* [45]. They showed that the scattering intensity from individual particles, without the interference term, assuming the classical LSW particle size distribution approaches q^{-4} with such oscillations. They also showed that the oscillations should become smaller as the particle size distribution function becomes broader. The existence of a secondary maximum in $s(q)$ has also been suggested theoretically by Tokuyama and Enomoto [33]. In their theory, the shape of the particles is assumed to be spherical at all times, but the secondary maximum is observed only at the late stage. However, the particle size distribution in their theory is a sharp Gaussian-like distribution at the intermediate stage and is nearly the same as our late-time results. Thus, it is unclear why no oscillations are predicted by their theory in the intermediate stage as well. They also suggest that the secondary maximum becomes more evident as volume fraction increases [50].

In Fig. 17, the amplitude of the oscillations at a volume fraction of 0.3 is much larger than that at a volume fraction of 0.1 (remember that Fig. 17 is a log-log plot). Fratzl [51] examined the particle size distribution dependence of the oscillations using Eq. (4.8), but fixed the value of $s(q)$ at $q = 0$ to be 1 for all distributions. The results shown in Fig. 17 are not normalized in this fashion. The values of $s(0)$ for the solid lines in Fig. 17 are about 0.7 and 2.7 at volume fractions of 0.1 and 0.3, respectively. If the results in Fig. 17 are normalized as Fratzl suggests, the magnitudes of the oscillations at both volume fractions become quite similar, since the difference between the two particle size distributions is small, as will be shown in Fig. 23. The peak heights of the structure functions in Fig. 17 are about 0.35 and 0.45 at volume fractions of 0.1 and 0.3, respectively. Thus, if the amplitude of the oscillations is compared with the peak height, the amplitude of the oscillations becomes larger as volume fraction increases. Oscillations in the structure function are usually not observed experimentally. However, some experiments show the oscillations clearly [26,52]. Thus, we conclude from our results that oscillations in the structure function are a generic characteristic of the coarsening process for systems composed of spherical particles.

Figure 18 shows the structure functions normalized by $s(q_m)$ where q_m is the wave number at which $s(q)$ is a maximum, versus q/q_m. The results using the monopole plus dipole approximation are shown for volume fractions of 0.1, 0.2, and 0.3. At a volume fraction of 0.05, the results using the monopole approximation are shown. Although the differences in the structure function between the monopole and monopole plus dipole approximations are small at a volume fraction of 0.1, the differences become larger as volume fraction increases. Since the monopole plus dipole approximation provides a much better description of the diffusion field at volume fractions exceeding 0.1 than does the monopole approximation, we only display the structure functions determined using the monopole plus dipole approximation. It is evident that the structure function becomes narrower as volume fraction increases. In order to compare the structure function with experiments and other theories, the full width at half maximum (FWHM) as a function of volume fraction is plotted in Fig. 19. The experimental results shown are Hennion *et al.* [18] (Al-Zn), Komura *et al.* [21] (Al-Zn), Guyot and Simon [19] (Al-Zn), Forouhi and de Fontaine [22] (Al-Zn), Hoyt and de Fontaine [23] (Al-Zn), Katano and Izumi [20] (Fe-Cr), Langmayr *et al.* [27] (Al-Ag) and Kraitchman *et al.* (Al-Li) (see Hoyt and de Fontaine [23]). The data points, except Langmayr *et al.*, are taken from Hoyt and de Fontaine [23] and Kostorz [53]. The theoretical curves shown are Rikvold and Gunton (RG) [28], Tokuyama and Enomoto (TE) [50], Hoyt and de Fontaine (HF) [23], and Fratzl and Lebowitz (FL) [54]. The RG and HF theories are based on a depletion zone model with a monodisperse particle system. The TE results are the solutions of a differential equation they derived for the structure function. FL derived an equation for the structure function using the asymptotic behavior of $s(q)$ at large q and assuming the asymptotic behavior of $s(q) \sim q^4$ at small q. The reason why the FL curve is not smooth is because they assumed that the morphology of the second phase varies with the volume fraction. Specifically, they assumed that the particles are spheres, rods, and plates at small, medium, and large volume fractions, respectively. Finally, our results are also shown and they agree well with the experimental measurement. In contrast to the FL theory, in our work the morphology of the second phase does not change with volume fraction. In addition, it is unlikely that the morphology of the second phase in all of the experiments shown in Fig. 19 is spherical. Nevertheless, the experimental data appear to agree well with an $s(q)$ determined using a self-consistent set of spatial correlations and particle size distributions.

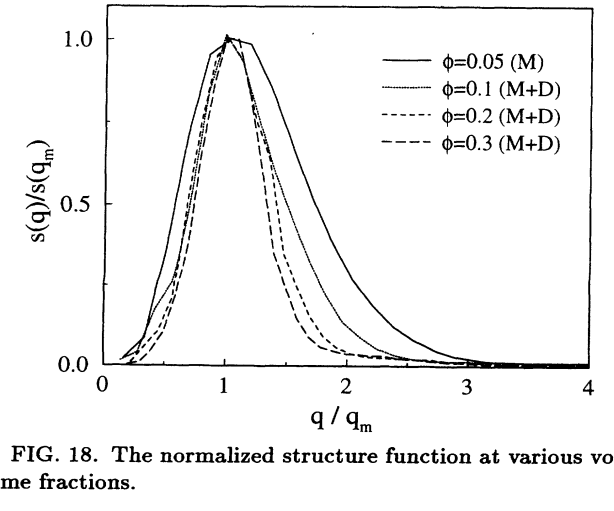

FIG. 18. The normalized structure function at various volume fractions.

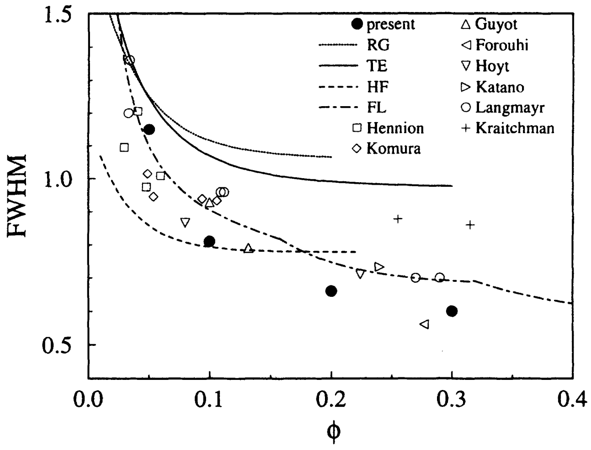

FIG. 19. The volume fraction dependence of the full width at half maximum (FWHM) of the structure function.

V. KINETICS

In the late stage, the cube of the average particle radius is expected to be proportional to time so that

$$\langle r\rangle^3 + C_0 = Kt \tag{5.1}$$

holds, where C_0 is a constant and K is the rate constant. Figure 20 shows the cube of the average particle size versus time at a volume fraction of 0.1. The large figure shows that the long-time evolution of $\langle r\rangle^3$ found using a single run is described well by a straight line. However, this is not true in the initial stage. Figure 20 also shows $\langle r\rangle^3$ as a function of time for $t < 10$ using the two different initial spatial distributions given by $d = 0$ and $d = 0.5$. The lines shown are not averaged results. Eight and four independent results for $d = 0$ and $d = 0.5$ are shown. At $t > 3$, the differences between the results using two different initial configurations of the system are clearly evident. If the results at $t < 3$ are magnified, slight deviations between the results are also noticeable. It is also obvious that the data points for $t < 6$ do not lie on a straight line. This is because the changes in the spatial correlation functions are drastic in this time range. In addition, the differences between the results with $d = 0$ and $d = 0.5$ are due to the different initial

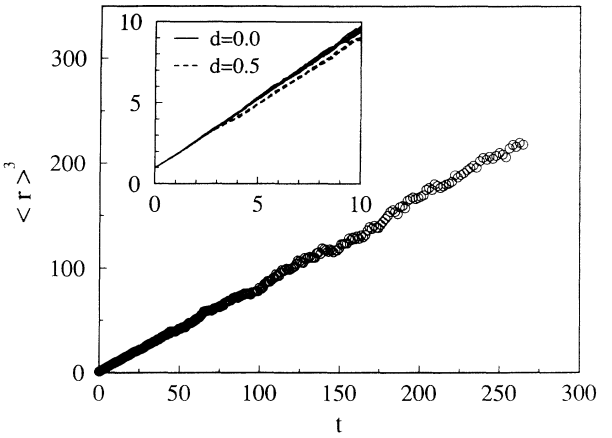

FIG. 20. The cube of average particle radius versus time at a volume fraction of 0.1 using the monopole approximation. Inset shows the short-time behavior of the cube of the average radius using the random spatial distributions with and without depletion zones.

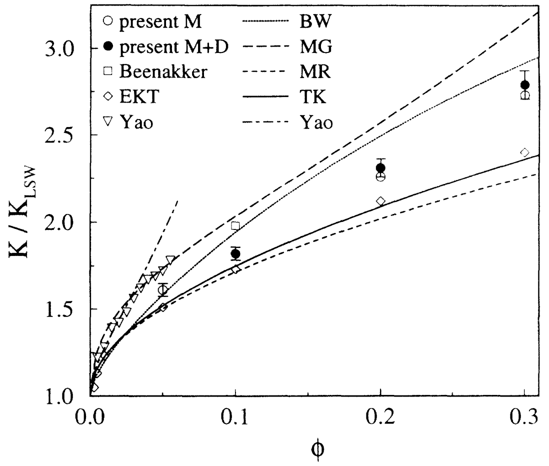

FIG. 21. The rate constant of the cubic growth rate K normalized to the LSW value as a function of volume fraction ϕ.

spatial distributions. Although the initial form of the spatial correlations affects the time dependence of $\langle r\rangle$ at early times, at long times these differences disappear, and a rate constant is obtained that is nearly identical for all the initial spatial distributions at a given volume fraction.

The rate constant was determined by calculating the slope of the line given by the cube of the average particle radius versus time using data in the range $23 < t < 240$. For times in this range, the number of particles in the system was typically 1000–100. As mentioned earlier the radial distribution functions become time independent when the number of particles is less than 1000, while the structure function at very low wave numbers displays a small time dependence. This time dependence is likely due to small changes in the particle spatial correlations. Nevertheless, this weak time dependence of the structure function appears to have no effect on the linearity of the $\langle r\rangle^3$ vs t data, and thus it is possible to use all the data in the range $23 < t < 240$ to determine the rate constant. This is consistent with the observation that, even when the structure function is strongly time dependent, the scaled particle size distribution is nearly time independent and the nonlinearity in a plot of $\langle r\rangle^3$ vs t is difficult to resolve. In addition, this larger time interval provides higher quality data, since the number of particles in the system is larger.

The rate constants of the cubic growth law, divided by the LSW value of 4/9, are shown in Fig. 21. The rate constants found through the numerical simulations of Beenakker [15], Enomoto, Kawasaki, and Tokuyama (EKT) [16], and Yao *et al.* [7], the mean-field theories of Brailsford and Wynblatt (BW) [5], Marsh and Glicksman (MG) [6], and Yao *et al.* [7], and the statistical mechanical theories of Marqusee and Ross (MR) [8], and Tokuyama, Kawasaki and Enomoto (TK) [10] are also shown in the figure. Beenakker employed a system of 5000 initial particles and the simulation method is similar to that used herein, but the number of particles in the interaction range was smaller. EKT employed a system of 10^5 initial particles but the simulation method is based on a one-dimensional model which is quite different from the present method. Yao *et al.*'s method is the same as Voorhees and Glicksman's method [14], but the initial number of particles was 1000. The monopole approximation was used in all of the above simulations. The BW result was obtained by approximating the average concentration field in a manner such that it satisfies a modified Helmholtz equation. The MG results are based on the self-similarity hypothesis and the assumption that a similar continuity equation holds for an interaction volume as well as for the particle volume. Yao *et al.*'s theory is similar to the BW theory, but a source term is added in the Helmholtz equation. However, this theory is valid only for volume fractions less than 0.06. MR and TK statistically averaged the concentration field, within the monopole approximation, and obtained results up to order of $\sqrt{\phi}$. As pointed out by Enomoto *et al.* [11] particle correlation effects are not included in the MR theory.

The mean-field approaches give higher rate constants and the statistical mechanical approaches give lower rate constants than the present results, except at a volume fraction of 0.05 where our results are quite close to that of BW. The simulation results of EKT agree well with the TK results; however, particle correlations are not taken into account in the EKT simulation. The rate constants of Beenakker and Yao *et al.* are higher than those of the present simulations. This is because the system size employed in their simulations was not sufficiently large to allow the two-phase mixture to reach the scaled time independent state and the rate constants were determined by regressing all of the $\langle r\rangle^3$ data obtained for a particular calculation. In particular, if we determine the rate constant by employing only the initial 200 values of $\langle r\rangle^3$ in our calculations, corresponding to $t < 5$, our results agree well with those of Beenakker and Yao *et al.* Also, if the data points at $t < 10$ are employed, the rate constants fall between the final and $t < 5$ values, indicating that the rate constant slowly decreased with time until the scaled time independent state was reached. As shown in Fig. 19, the structure function of TE theory is much broader than that of the present results. Thus, the difference in the rate constants predicted by the TK theory and us at high volume fractions may be due to the differences in the particle spatial correlations predicted by TK and us. One possible reason for the difference in the spatial correlations predicted by the TK theory and those found in our simulations is that the TK theory is correct only up to the order of the square root of the volume fraction, and thus at higher volume fractions higher order terms may have to be included in the theory. In general the rate constants determined using the dipole approximation are only slightly higher than that found using the monopole approximation. Therefore, the addition of dipole terms appears to have a large effect on the spatial correlations at high volume fractions, but a comparatively small effect on the rate constant despite the large fraction of overlapping particles when the monopole approximation is employed. In Fig. 21, Marder's results are not shown, because his rate constants are larger than all those shown by approximately a factor of 10. Unfortunately, a comparison of these theories with experimental results is not possible. The experiments are usually performed at higher volume fractions, and for many cases the material constants required to calculate the rate constants are not known.

Consistent with earlier work [42], there is a distribution of growth rates for a particle of a given size and the width of this distribution depends on ρ, where $\rho = r/\langle r\rangle$. At lower values of ρ, the fluctuations in the growth rate are smaller than at large ρ because, as mentioned earlier, smaller particles do not interact as strongly with their neighboring particles as do large particles. Although the presence of fluctuations in the growth rate is well documented, we now have sufficient data to determine how these fluctuations are distributed for a given particle size class. Figure 22 shows the distribution of the growth rates, $h(b_{00})$, in the range $0.95 < \rho < 1.05$ at a volume fraction of 0.1 which was determined using the monopole approximation. In this case $\int_{-\infty}^{\infty} h(b_{00})db_{00} = 1$. The distribution of growth rates in the scaling region and that of a random spatial distribution for both $d = 0.0$ and $d = 0.5$ are shown. The particles with negative b_{00} are particles which are surrounded locally by larger particles, and particles with positive b_{00} are particles which are surrounded by smaller particles. As shown in Fig. 22, the distributions of the growth rates are almost identical in the late stage. At $t = 0$ the initial particle distribution with $d = 0$ produces a broader range of growth rates than that produced with $d = 0.5$. This is because, as shown in Figs. 7–10, the particle density near a particle is higher for a random distribution with $d = 0$ than that found with either the distribution produced using $d = 0.5$ or in the long-time limit. It is also clear from Fig. 22 that fluctuations in the growth rate about the mean are not symmetrically distributed; there are more particles with large positive growth rates than particles with negative growth rates of the same magnitude. The asymmetry in the distribution of growth rates may be due the fact that in the low volume fraction limit where the monopole approximation is valid, the effect of a particle on another particle's growth rate is simply related to the distance between the centers of the particles. From geometrical considerations, it is clear that it is possible to place more smaller particles around a particle of a given size than it is to place large particles around this same particle and, in addition, the centers of these small particles will be closer to this particle than the centers of the large particles. As the smaller particles are closer to a given particle and their number density may be higher, it is easier to obtain particles with large positive growth rates than particles with negative growth rates of the same magnitude.

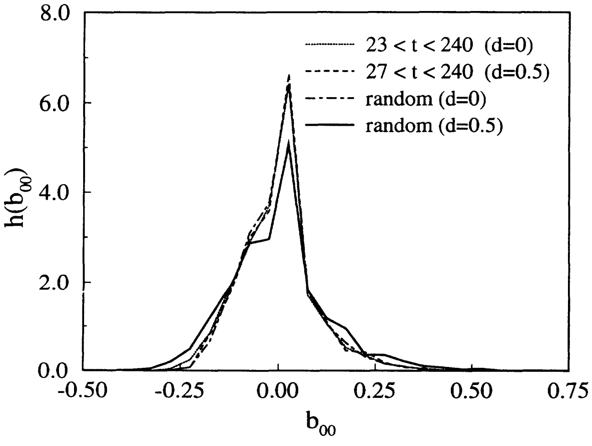

FIG. 22. The distribution of the growth rate in the range $0.95 < \rho < 1.05$ at a volume fraction of 0.1.

The scaled particle size distribution, $f(\rho)$, is obtained by averaging the particle radii at twelve different times in the late stage. As mentioned earlier, we employed an initial particle size distribution which was the particle size distribution of a previous run at the same volume fraction, and the scaled particle size distribution function did not change, to within the scatter of the data, as the spatial correlations were developing. Since the spatial correlation functions are time dependent at the initial and intermediate stages, we conclude that the particle size distribution function is not a strong function of the particle spatial correlations in this range of volume fraction. Figure 23 shows the volume fraction dependence of the particle size distribution function. The results using the monopole plus dipole approximation, except at a volume fraction of 0.05, are shown. As mentioned earlier, the addition of the dipole terms has a small effect on the rate constant. This is also the case for the particle size distribution. The distribution function becomes broader as volume fraction increases. We find that the volume fraction dependence of the distribution function is not strong. However, the difference between the LSW distribution and the distribution function at a volume fraction of 0.05 is large. This large change in the distribution function at small volume fractions indicates that the LSW distribution is quite unrealistic for nonzero volume fraction systems. Fig. 24 compares the particle size distribution function at a volume fraction of 0.1 with the results of other workers. Only the results of MR and TK are shown so that it is possible to resolve the small differences between the distributions. The BW distribution function has about the same peak height as the MR result but it occurs at smaller ρ and is a bit narrower. The

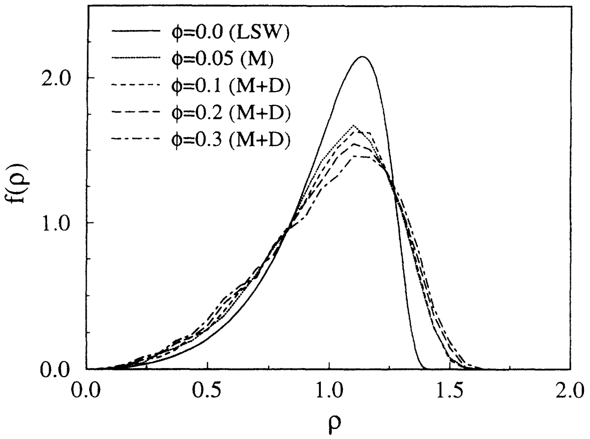

FIG. 23. Volume fraction dependence of the scaled particle size distribution function.

MG distribution function lies between the MR and TK results. Although the TK distribution function is the closest to the present results, it is difficult to conclude much via a comparison of distribution functions due to the large amount of data necessary to produce a smooth distribution function, and small differences between the various theoretical predictions. As mentioned earlier the effect of particle spatial correlations on the rate constant is small at a volume fraction of 0.1. This is also the case for the particle size distributions at a volume fraction 0.1, as the MR theory neglects spatial correlations entirely.

VI. CONCLUSIONS

Large-scale numerical simulations of the coarsening process in two-phase mixtures were performed. A method was developed to solve the multiparticle diffusion problem to an arbitrary degree of precision, assuming that the particles are spherical. Using this solution to the multiparticle diffusion problem, simulations were performed using both monopole and monopole plus dipole approximations. On the basis of these calculations we can conclude the following:

(i) The commonly used monopole approximation is valid up to a volume fraction of about 0.1. At volume fractions in excess of 0.1 dipole terms must be employed to determine the diffusion field in the matrix. These dipole terms have a small effect on the value of the rate constant, but a large effect on the structure function and the spatial correlations. These results also show that at volume fractions exceeding 0.1 particle migration is an essential aspect of the coarsening process, and that significant particle overlap occurs if these particle migrations are neglected.

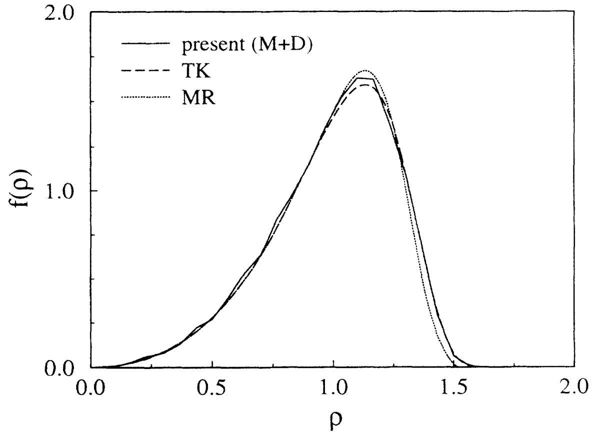

FIG. 24. The scaled particle size distribution function at a volume fraction of 0.1, compared with the TK and MR results.

(ii) Unique volume fraction dependent spatial correlations will be present in the late stage. These spatial correlations are quite different from those of the random distributions created either with or without depletion zones surrounding a particle. In the scaling regime large depletion zones exist between small particles. The size of the depletion zones becomes smaller as the size of the particles increases, and depletion zones are not present between large particles. The probability of finding small particles in the immediate vicinity of large particles is lower than that of a random spatial distribution with no depletion zones. This is due to the strong diffusional interaction between a small and large particle when they are located near one another.

(iii) The temporal evolution of these spatial correlations, both with and without depletion zones, induced a significant time dependence in the shape of the scaled structure function. Nevertheless, after sufficient time, the scaled structure functions assumed a time independent form regardless of the initial spatial arrangement of the particles employed in the calculation.

(iv) At small wave numbers the slope of the structure function in a log-log plot appears to approach 4. The slope of the structure function at very large wave numbers is -4, but oscillations in the structure function were observed at large wave numbers. The shape of the structure function at large wave numbers, and these oscillations can be described well by assuming that the structure function is given by the particle size distribution function and the form factor for a sphere.

(v) The experimentally observed volume fraction dependence of the full width at half maximum of the scaled structure function agrees well with our calculations. This suggests that an accurate description of both the particle size distribution function and the particle spatial correlation functions is necessary to predict the structure function.

(vi) The amplitude of the temporal power law for the average particle radius changes by about a factor of 2 over a volume fraction range of 0.05–0.3. The monopole plus dipole approximation yielded slightly higher rate constants than those given by the monopole approximation.

(vii) Fluctuations in the growth rate of a particle of a given size, which result from variations in the local environment of a particle, are not distributed symmetrically about the average growth rate of particles in this size class.

ACKNOWLEDGMENTS

This work was supported by NASA Microgravity Science and Applications Division under Grant No. NAG8-769.

APPENDIX

Spherical harmonics of an argument with a sum of two vectors can be expanded into a sum of the products of two spherical harmonics of the vectors in two ways [39,55–58],

$$\begin{aligned} |\mathbf{R}_j+\mathbf{R}_k|^n\, Y_n^m(\mathbf{R}_j+\mathbf{R}_k) &= \sum_{n'=0}^{n}\sum_{m'=-n'}^{n'} R_j^{n-n'} R_k^{n'} \begin{pmatrix} n+m \\ n'+m' \end{pmatrix} \\ &\quad \times Y_{n-n'}^{m-m'}(\mathbf{R}_j)\, Y_{n'}^{m'}(\mathbf{R}_k). \end{aligned} \tag{A1}$$

$$\begin{aligned} \frac{1}{|\mathbf{R}_j+\mathbf{R}_k|^{n+1}} Y_n^m(\mathbf{R}_j+\mathbf{R}_k) &= \sum_{n'm'}(-1)^{m'} \frac{R_k^{n'}}{R_j^{n+n'+1}} K(n,-m;n',-m') \\ &\quad \times Y_{n+n'}^{m-m'}(\mathbf{R}_j)\, Y_{n'}^{m'}(\mathbf{R}_k) \\ &\quad (R_j > R_k). \end{aligned} \tag{A2}$$

The primary difference between these expressions is that the summation in the right-hand side of Eq. (A1) is truncated at $n = n'$, but the summation in Eq. (A2) goes to infinity. Also, there are no restrictions for R_j and R_k in Eq. (A1), but $R_j > R_k$ in Eq. (A2). Equations (A1) and (A2) are useful formulas; however, these are not widely known.

Using Eq. (A2), changing indices in Eq. (A2) m to $-m$ and m' to $-m'$, Eq. (2.30) can be expanded into a series of products of three spherical harmonics,

$$\begin{aligned} g(\mathbf{p},\mathbf{q}) &= \frac{1}{|\mathbf{r}_j-\mathbf{r}_k-\mathbf{d}_{jk}|} \\ &= \sum_{nm}(-1)^m \frac{r_j^n}{|\mathbf{r}_k+\mathbf{d}_{jk}|^{n+1}} Y_n^{-m}(\mathbf{r}_k+\mathbf{d}_{jk})\, Y_n^m(\mathbf{r}_j) \\ &= \sum_{nm}\sum_{n'm'}(-1)^{m+m'} K(n,m;n',m') \frac{r_j^n r_k^{n'}}{d_{jk}^{n+n'+1}} \\ &\quad \times Y_{n+n'}^{-m+m'}(\mathbf{d}_{jk})\, Y_n^m(\mathbf{r}_j)\, Y_{n'}^{-m'}(\mathbf{r}_k). \end{aligned} \tag{A3}$$

The variables are separated in Eq. (A3) so that integration can be performed easily.

[1] I. M. Lifshitz and V. V. Slyozov, J. Phys. Chem. Solids **19**, 35 (1961).

[2] C. Wagner, Z. Elektrochem. **65**, 581 (1961).

[3] S. C. Hardy and P. W. Voorhees, Metall. Trans. A **19**, 2713 (1988).

[4] A. J. Ardell, Acta Metall. **20**, 61 (1972).

[5] A. D. Brailsford and P. Wynblatt, Acta Metall. **27**, 489 (1979).

[6] S. P. Marsh and M. E. Glicksman, in *Modeling of Coarsening and Grain Growth*, edited by S. P. Marsh and C. S. Pande (TMS, Warrendale, 1992).

[7] J. H. Yao, K. R. Elder, H. Guo, and M. Grant, Phys. Rev. B **47**, 14 110 (1993).

[8] J. A. Marqusee and J. Ross, J. Chem. Phys. **80**, 536 (1984).

[9] M. Tokuyama and K. Kawasaki, Physica A **123**, 386 (1984).

[10] M. Tokuyama, K. Kawasaki, and Y. Enomoto, Physica A **134**, 323 (1986).

[11] Y. Enomoto, M. Tokuyama, and K. Kawasaki, Acta Metall. **34**, 2119 (1986).

[12] M. Marder, Phys. Rev. A **36**, 858 (1987).

[13] P. W. Voorhees and M. E. Glicksman, Acta Metall. **32**, 2001 (1984).

[14] P. W. Voorhees and M. E. Glicksman, Acta Metall. **32**, 2013 (1984).

[15] C. W. J. Beenakker, Phys. Rev. A **33**, 4482 (1986).

[16] Y. Enomoto, K. Kawasaki, and M. Tokuyama, Acta Metall. **35**, 907 (1987).

[17] M. Marder, Phys. Rev. Lett. **55**, 2953 (1985).

[18] M. Hennion, D. Ronzaud, and P. Guyot, Acta Metall. **30**, 599 (1982).

[19] P. Guyot and J. P. Simon, in *Solid-Solid Phase Transformations*, edited by H. I. Aaronson, D. E. Laughlin, R. F. Sekerka, and C. M. Wayman (TMS, Warrendale, 1982), pp. 325–345.

[20] S. Katano and M. Izumi, Phys. Rev. Lett. **52**, 835 (1984).

[21] S. Komura, K. Osamura, H. Fujii, and T. Takeda, Phys. Rev. B **31**, 1278 (1985).

[22] A. R. Forouhi and D. de Fontaine, Acta Metall. **35**, 1863 (1987).

[23] J. J. Hoyt and D. de Fontaine, Acta Metall. **37**, 1611 (1989).

[24] S. Abis *et al.*, Phys. Rev. B **42**, 2275 (1990).

[25] E. Caponetti, E. M. D'Aguanno, R. Triolo, and S. Spooner, Philos Mag. B **63**, 1201 (1991).

[26] P. Fratzl, Y. Yoshida, G. Vogl, and H. G. Haubold, Phys. Rev. B **46**, 11 323 (1992).

[27] F. Langmayr, P. Fratzl, and G. Vogl, Acta Metall. **40**, 3381 (1992).

[28] P. A. Rikvold and J. D. Gunton, Phys. Rev. Lett. **49**, 286 (1982).

[29] R. Triolo, E. Caponetti, and S. Spooner, Phys. Rev. B **39**, 4588 (1989).

[30] J. S. Pedersen, Phys. Rev. B **47**, 657 (1993).

[31] O. Krichevsky and J. Stavans, Phys. Rev. Lett. **70**, 1473 (1993).

[32] M. Tokuyama, Y. Enomoto, and K. Kawasaki, Physica A **143**, 183 (1987).

[33] M. Tokuyama and Y. Enomoto, Phys. Rev. E **47**, 1156 (1993).

[34] C. W. J. Beenakker and J. Ross, J. Chem. Phys. **84**, 3857 (1986).

[35] T. A. Abinandanan and W. C. Johnson, Acta Metall. **41**, 27 (1993).

[36] T. A. Abinandanan and W. C. Johnson, Acta Metall. **41**, 17 (1993).

[37] T. Imaeda and K. Kawasaki, Physica A **186**, 359 (1992).

[38] M. A. Jaswon and G. T. Symm, *Integral Equation Methods in Potential Theory and Elastostatics* (Academic, London, 1977).

[39] N. Akaiwa, Ph.D. thesis, Northwestern University, 1993.

[40] W. J. Sternberg and T. L. Smith, *The Theory of Potential and Spherical Harmonics* (The University of Toronto Press, Toronto, 1944).

[41] G. B. McFadden, P. W. Voorhees, R. F. Boisvert, and D. I. Meiron, J. Sci. Comput. **1**, 117 (1986).

[42] P. W. Voorhees, G. B. McFadden, R. F. Boisvert, and D. I. Meiron, Acta Metall. **36**, 207 (1988).

[43] J. A. Given, J. Blawzdziewicz, and G. Stell, J. Chem. Phys. **93**, 8156 (1990).

[44] G. Porod, in *Small Angle X-ray Scattering*, edited by O. Glatter and O. Kratky (Academic, London, 1982), pp. 17–51.

[45] P. Fratzl, J. L. Lebowitz, O. Penrose, and J. Amar, Phys. Rev. B **44**, 4794 (1991).

[46] C. Yeung, Phys. Rev. Lett. **61**, 1135 (1988).

[47] Y. Oono and S. Puri, Phys. Rev. A **38**, 434 (1988).

[48] H. Furukawa, J. Phys. Soc. Jpn. **58**, 216 (1989).

[49] A. Shinozaki and Y. Oono, Phys. Rev. Lett. **66**, 173 (1991).

[50] M. Tokuyama and Y. Enomoto (unpublished).

[51] P. Fratzl, J. Appl. Crystallogr. **24**, 593 (1991).

[52] P. Wiltzius (private communication).

[53] G. Kostorz, J. Appl. Crystallogr. **24**, 444 (1991).

[54] P. Fratzl and J. L. Lebowitz, Acta Metall. **37**, 3245 (1989).

[55] F. D. Wette and B. Nijboer, Physica **24**, 1105 (1958).

[56] C. G. Gray, Can. J. Phys. **46**, 135 (1967).

[57] D. McKenzie, R. McPhedran, and G. Derrick, Proc. R. Soc. London, Ser. A **362**, 211 (1978).

[58] B. Felderhof, Physica A **130**, 34 (1985).